UT GSBS Dissertations and Theses (Open Access)   Graduate School of Biomedical Sciences

8-2013

Renal Cryoablation: Investigation of Periprocedural Visualization Tools and Treatment Response Quantification

Katherine L. Dextraze

Follow this and additional works at: http://digitalcommons.library.tmc.edu/utgsbs_dissertations

Part of the Medicine and Health Sciences Commons, Numerical Analysis and Scientific Computing Commons, and the Survival Analysis Commons

The TMC LIBRARY
Health Sciences Resource Center

RENAL CRYOABLATION: INVESTIGATION OF PERIPROCEDURAL

VISUALIZATION TOOLS AND TREATMENT RESPONSE

QUANTIFICATION

by

Katherine Louise Dextraze, BS

APPROVED:

_____
Supervisory Professor
R Jason Stafford, PhD

_____
John Hazle, PhD

_____
Dr. Ping Hou, PhD

_____
Dr. Arvind Rao, PhD

_____
Donna Reeve, MS

APPROVED:

_____
Dean, The University of Texas
Graduate School of Biomedical Sciences at Houston

RENAL CRYOABLATION: INVESTIGATION OF PERIPROCEDURAL

VISUALIZATION TOOLS AND TREATMENT RESPONSE

QUANTIFICATION

A
THESIS

Presented to the Faculty of
The University of Texas
Health Science Center at Houston
and
The University of Texas
MD Anderson Cancer Center
Graduate School of Biomedical Sciences
in Partial Fulfillment

of the Requirements

for the Degree of

MASTER OF SCIENCE

by

Katherine Louise Dextraze, BS
Houston, Texas

August, 2013

Acknowledgements

RENAL CRYOABLATION: INVESTIGATION OF PERIPROCEDURAL VISUALIZATION TOOLS AND TREATMENT RESPONSE QUANTIFICATION

Publication No._____*

Katherine Louise Dextraze, MS

Supervisory Professor: R Jason Stafford, Ph.D.

Cryoablation for small renal tumors has demonstrated sufficient clinical efficacy over the past decade as a non-surgical nephron-sparing approach for treating renal masses for patients who are not surgical candidates. Minimally invasive percutaneous cryoablations have been performed with image guidance from CT, ultrasound, and MRI. During the MRI-guided cryoablation procedure, the interventional radiologist visually compares the iceball size on monitoring images with respect to the original tumor on separate planning images. The comparisons made during the monitoring step are time consuming, inefficient and sometimes lack the precision needed for decision making, requiring the radiologist to make further changes later in the procedure. This study sought to mitigate uncertainty in these visual comparisons by quantifying tissue response to cryoablation and providing visualization of the response during the procedure.

Based on retrospective analysis of MR-guided cryoablation patient data, registration and segmentation algorithms were investigated and implemented for periprocedural visualization to deliver iceball position and size with respect to planning images registered within 3.3mm with at least 70% overlap. A quantitative logit model was developed to relate perfusion deficit in renal parenchyma visualized in verification images as a result of iceball size visualized in monitoring images.

Through a retrospective study of 20 patient cases, the relationship between the likelihood of perfusion loss in renal parenchyma and distance within the iceball was quantified and iteratively fit to a logit curve. Using the parameters from the logit fit, the margin for 95% perfusion loss likelihood was found to be 4.28 mm within the iceball. The observed margin corresponds well with the clinically accepted margin of 3-5mm within the iceball.

In order to display the iceball position and perfusion loss likelihood to the radiologist, algorithms were implemented to create a fast segmentation and registration module which executed in under two minutes, within the clinically-relevant three minute monitoring period. Using sixteen patient cases, the average Hausdorff distance was reduced from 10.1mm to 3.21 mm with average Dice Similarity Coefficient increased from 46.6% before registration to 82.6% after registration.

Abbreviations

AIR: Automated Image Registration; a software package

BEAT: a balanced steady state free precession sequence available from Siemens Healthcare whose acquisition parameters can be tailored in real-time

bssFP: balanced steady state free precession MRI sequence

CDF: cumulative distribution function

CT: Computed Tomography

DICOM: Digital Imaging and Communications in Medicine; a digital standard for handling, storing, printing, and transmitting medical information and images in 2D and 3D

DSC: Dice Similarity Coefficient

(F)FT: (fast) Fourier Transform

glmfit: generalized linear model fitting function available through MATLAB

HASTE: a single-shot fast spin echo sequence available through Siemens Healthcare

HD: Hausdorff distance

HIFU: High Intensity Focused Ultrasound

ICP: Iterative Closest Point; an approach to image registration

MRI: Magnetic Resonance Imaging

(N)MI: (normalized) Mutual Information; an optimization metric for automated image registration

NRRD: "nearly raw raster data; a library and file format which supports n-dimensional data

RCC: Renal Cell Carcinoma

RF: Radiofrequency

STAPLE: Simultaneous Truth and Performance Level Estimation; for statistically estimating ground truth segmentation from a series of trials

ssFSE: single shot fast spin echo

T1: an nuclear magnetic resonance parameter which describes spin-lattice relaxation

T2: nuclear magnetic resonance parameter which describes spin-spin relaxation

trueFISP: a balanced steady state free precession sequence available from Siemens Healthcare

VIBE: a dynamic four-phase series of contrast-enhanced T1-weighted acquisitions

Contents

List of Figures

1 Project Statement and Specific Aims

Cryoablation for small renal tumors has demonstrated sufficient clinical efficacy over the past decade as a non-surgical nephron-sparing approach for treating patients who are not surgical candidates. By eliminating surgical resection, percutaneous and laparoscopic cryoablations have reduced procedural impact on the patient from the co-morbidities and complications associated with a standard surgical approach [1]. Minimally invasive percutaneous cryoablations are now routinely performed in an outpatient setting using image guidance from CT, ultrasound, or MRI. MRI stands out as the only modality that allows for visualization of the extent of disease and of the surrounding anatomy as well as high contrast visualization of the complete extent of the iceball during the procedure.

The MRI-guided percutaneous cryoablation procedure involves four major imaging steps: a planning acquisition to localize the tumor, guidance for placing the cryoablation probes into the target tissue, monitoring of the iceball created by the probes, and evaluation to immediately determine if the tumor was effectively ablated. During the monitoring interval, the interventional radiologist visually compares the iceball size on monitoring images with respect to the original tumor on planning images. The comparison requires flipping among several data sets, which are not aligned spatially. The interventional radiologist uses this comparison to effectively treat the tumor by visually estimating a 3-5mm margin of iceball extending beyond the target lesion which purportedly corresponds to the -20˚C isotherm in the iceball[2].The growing iceball creates a signal deficit which obscures the kidney and target lesion. The image series may be misaligned due to patient or prescription positioning as well as obscuring of the anatomy by the iceball. The comparisons made during the monitoring step are time consuming, inefficient and sometimes lack the precision needed for decision making, requiring the radiologist to make further changes during a second freeze cycle, such as adding a cryoprobe to mitigate the uncertainty.

Using retrospective analysis of previously performed MR-guided cryoablations in patients, we hypothesize that it is feasible to develop a software tool for periprocedural visualization to deliver iceball position and size with respect to planning images registered within 3.3mm with at least 70% overlap as well as develop a quantitative logit model relating the visualized iceball edge to the perfusion deficit in the renal parenchyma to aid in margin assessment.

To achieve this hypothesis, this project specifically aimed to:

SA1) **Employ logit analysis on carefully selected and registered images from previously performed MR-guided cryoablation procedures in patients to quantify the likelihood of perfusion loss as a function of distance within the visible iceball on the monitoring images as assessed by T1-weighted contrast-enhanced post-treatment imaging .**

SA2) **Investigate, implement and validate a fast approach to segmentation of the iceball with automated rigid registration to the planning images for assessing treatment progression and displaying perfusion loss probability from the quantitative model.**

2   Background

2.1 Renal Cell Carcinoma

The recent rise in the number of diagnostic imaging procedures performed has resulted in increased detection of small renal lesions as incidental findings. These small masses are typically detected in patients over 60 years old [3]. These cases, which include a population with compromised health, have encouraged development of treatments with decreased morbidity compared with the traditional regimens of open partial nephrectomy, radiation therapy, and chemotherapy. Minimally invasive image-guided percutaneous

cryoablation techniques for small renal cell carcinoma tumors have shown good clinical success over the past decade, offering a less invasive method of treating renal masses [4].

For diagnosis of the renal mass after detection, contrast-enhanced CT or MRI is performed to characterize the mass. Percutaneous biopsy is indicated if the mass is suspected of being a metastasis. Renal cell carcinoma accounts for about 80% of diagnoses of primary small renal masses. Patients with RCC are often asymptomatic, which is why this disease is frequently found incidentally. Renal cell carcinoma (RCC) is highly resistant to radiation and typical chemotherapy, such that surgery and ablation are the most clinically effective methods for managing the disease [2].

2.1.1 Established Ablative Therapies for Localized Tumor Control of Renal Cell Carcinoma

Two non-surgical methods have been established to achieve localized tumor control in renal tissue: radiofrequency (RF) ablation and cryoablation. RF achieves ablation by heating the target tissue to at least 60^0C in order to induce necrosis, while cryoablation destroys tissue by freezing [2]. These ablative therapies are less invasive than standard surgery, resulting in a shortened recovery time for the patient. Compared to radiation therapy, ablation reduces side effects in healthy tissue and the ablative procedure can be performed during a single patient visit, rather than several weeks of fractionated treatment for radiation therapy. For renal ablation procedures, RF and cryoablation procedures can be performed either percutaneously (with image guidance) or laparoscopically [2]. Laparoscopic procedures require general anesthesia and result in an overnight stay for the patient, whereas percutaneous ablation procedures are typically outpatient procedures which require only conscious sedation and result in fewer complications than laparoscopic procedures. The local recurrence rate following cryoablation with repeated freeze/thaw cycles is below 2%, while local recurrence rates using RF ablation have been reported to

be 10% or more [2]. The higher recurrence rate of RF ablation is likely due to the lack of perioperative monitoring and margin visualization.

Percutaneous cryoablation is typically indicated under the following circumstances [2,5]:

- Tumor diameter < 4cm, limited to kidney tissue

- Patient has low tolerance for surgery due to comorbidities, prior abdominal surgeries, and age.

- Nephron preservation is necessary for patients with a single kidney or multiple tumors are present

2.1.2 MRI-guided Cryoablation

Percutaneous cryoablation was first proposed as an alternative to nephrectomy in 1995[6]. Uchida, et al. studied the effectiveness of cryoablation on renal cancer cell cultures and excised canine kidney before performing cryoablation on patients under CT guidance. From the canine study, it was determined that cryoablation of renal cancer cells needs to achieve temperatures below -20ºC to be cytotoxic. For patient studies, perfusion loss was assessed by measuring the non-enhancing region of kidney tissue as shown on iodine contrast-enhanced CT.

Advantages of MRI

MRI stands out as the only modality that allows for visualization of the extent of disease and surrounding anatomy, as well as high contrast visualization of the complete extent of the iceball during the procedure. MRI is capable of acquiring these images in an arbitrarily oriented anatomic plane, which minimizes the need for patient repositioning and post-processing computation. A comparison of iceball visualization on CT and MRI is illustrated in Figure 1 [7]. Although CT acquisitions are faster and capable of finer spatial resolution,

CT still requires ionizing radiation, does not offer high quality soft tissue contrast or iceball contrast, and relies on intensive post-processing for the visualization of oblique planes.

(a)   (b)
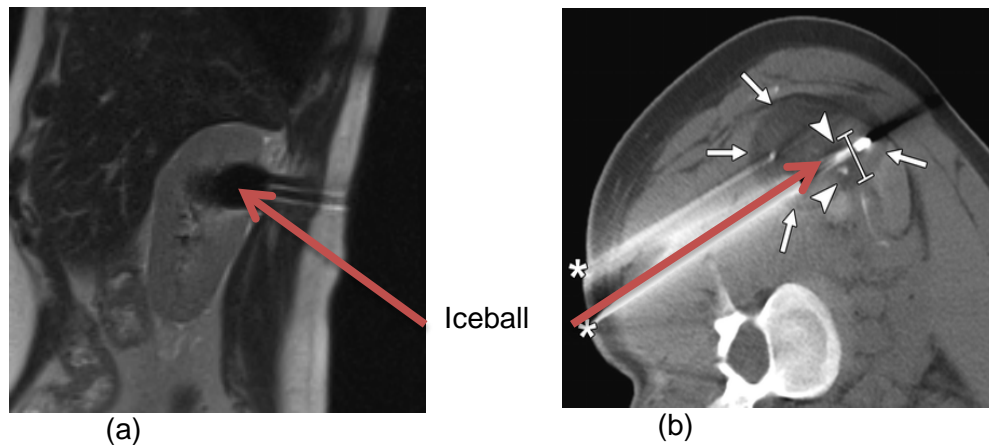
Figure 1: Advantages of ice ball visualization and soft tissue contrast in MRI- versus CT-guided cryoablations (a) Sagittal T2-weighted single shot fast spin echo acquired for iceball monitoring after 12 minutes of freeze time; iceball is hypointense and well-defined; surrounding abdominal soft tissue is well differentiated between organs and surrounding fat. (b) CT-guided cryoablation intraprocedural axial CT acquired after 10 minutes of freeze time[7]; iceball is not well-defined; needle artifacts are bright; surrounding soft tissue shows poor contrast with organs and iceball.

Stronger gradients and multi-channel phased-array receivers for MRI allow for pulse sequences that facilitate fast image acquisition while maintaining excellent soft tissue contrast with only modest reductions in signal to noise ratio and resolution. Development of MR-compatible equipment has further expanded the role of MRI in image-guided procedures, such that this soft tissue contrast can be exploited for more accurate planning, targeting, monitoring, and post-treatment evaluation of procedures such as renal cryoablation.

MRI-Compatible Cryoablation Equipment

At The University of Texas MD Anderson Cancer Center, percutaneous cryoablations are performed under image guidance from the interventional MR scanner (1.5T Magnetom Espree; Siemens Healthcare; Erlangen, Germany). The system has a wide bore (70 cm) which accommodates a variety of patient sizes, positioning and interventional equipment, as well as a short length (124 cm) which facilitates the ability to reach into the magnet

during the acquisition and manipulate instruments under real-time MRI-guidance.
Standard diagnostic phased array coils were used, including a spine array insert and a 6-channel body matrix array with openings for probe insertion. The patients are placed aneasthetized and typically placed in a prone position to accomodate access to the kidney [4].

In planning, the diameter of the gross tumor volume determines the total number of probes that will be needed to perform a successful ablation, approximately one probe per centimeter of tumor [8]. The MR-compatible probes are part of a system designed to function in the MRI (IceRod ® and MRI-compatible cryoablation system; Galil Medical Inc., Arden Hills, MN). The face of the unit and one elliptical probe are shown in Figure 2.

(a) Argon and Helium gas-center cryoablation system (MRI-compatible cryoblation system, Galil Medical Inc., Arden Hills, MN)
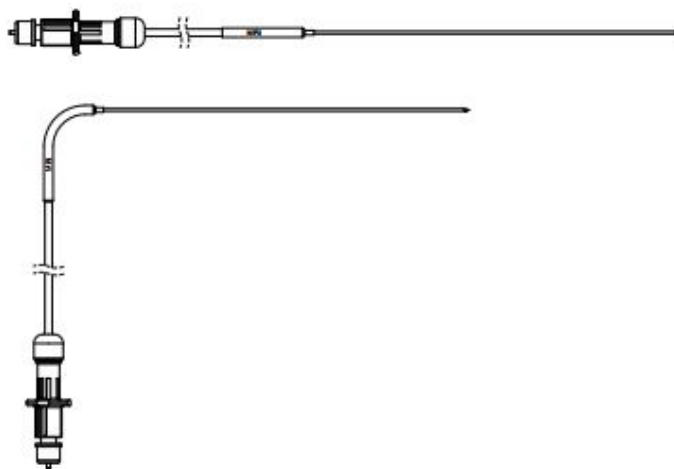
(b) 17-gauge Percutaneuos Cryoablation Probe (IceRod ®Galil Medical Inc., Arden Hills, MN)

Figure 2: MR-compatible cryoablation equipment: a gas-center unit capable of accommodating 25 cryoablation needles and nickel-chromium flexible 17-gauge cryoablation needle

To achieve very low temperatures, these cryoablation probes rely on the Joule-Thompson effect in which the temperature of a liquid or gas changes as a result of being forced through a valve. Highly compressed argon gas is directed through the probes and, as the gas rapidly expands, it cools, resulting in an iceball that forms from water natively present in the tissue. The freeze step lasts about 10-15 minutes and is followed by an active thaw period, in which Helium gas, which heats upon expansion, is directed through the cryoprobes. The freeze-thaw cycle is repeated at least twice to increase efficacy. Cell death from cryoablation occurs on two time scales: immediately, due to the intracellular response to the freeze/thaw cycles and to edema, and in the days following the therapy, due to platelet aggregation and vascular thrombosis [1]. These acute and permanent responses of the tissue are outlined in Figure 3. Edema and platelet aggregation most likely the mechanisms that allow for visualization of damage on contrast-enhanced imaging acquisitions.
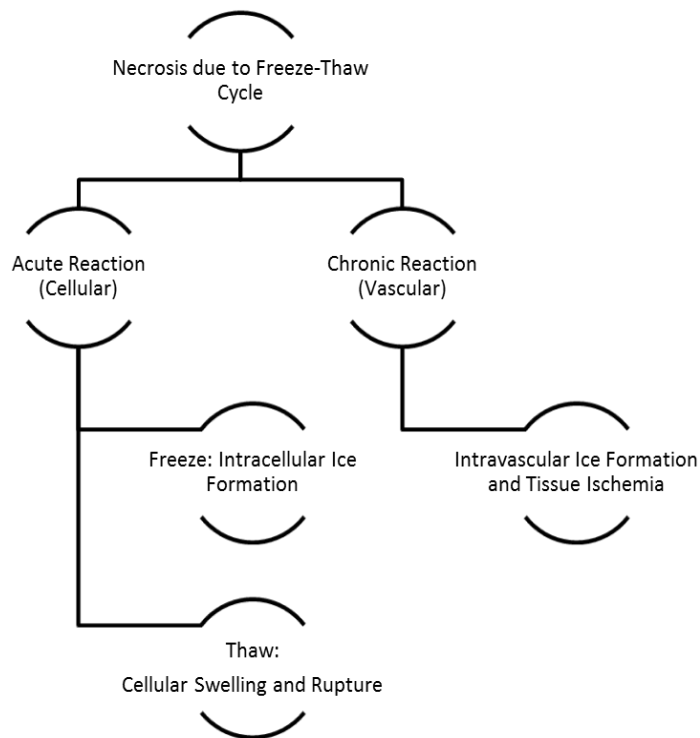
Figure 3: Acute and Chronic Response of Tissue following Cryoablation. Acute response incites edema and platelet recruitment, mechanisms which disrupt blood flow and lead to ischemia. Chronic response leads to tissue ischemia, followed by eventual lesion reabsorption in successful ablation cases.

Tissue necrosis and treatment margins have previously been evaluated by histological methods. However, MRI sequences offer non-invasive options for visualizing tissue damage following cryoablation. Van den Bosch, et al. assessed the reliability of MR-guidance by comparing the MR-visualized non-perfused area in cryoablated canine prostates against the necrotic area measured by histology after resection [9]. This study found that the visualization of the necrotic region using standard MRI contrast mechanisms depends heavily on the choice of pulse sequence. For post-ablation assessment using a contrast-enhanced spoiled gradient-recalled echoT1-weighted image, the low signal area of tissue matched the area of cell death measured in histology within 6%. Therefore, to assess visualized tissue damage, this study relied on T1-weighted contrast-enhanced (T1+C) sequences acquired immediately following treatment.

Cryoablation Procedure and Periprocedural Monitoring

At UT MD Anderson, the patient is breath-held during all acquisitions. Image acquisition during cryoablation can be grouped into four stages:

(1) Planning: Lesion identification and probe entry planning, shown in Figure 6.

(2) Targeting: Guidance of cryoprobes to the target tissue, typically with real-time acquisitions.

(3) Monitoring: Probe localization and iceball monitoring, shown in Figure 7.

(4) Evaluation: Visualization of tissue necrosis immediately following cryoablation (by Gadolinium contrast-enhancement and/or diffusion-subtraction imaging), shown in Figure 8.

During planning, the target lesion is typically identified using a balanced steady state free precession sequence (bssFP), known as true fast imaging with steady state precession

(trueFISP) on the Siemens platform. This acquisition can be made with or without a chemically selective saturation technique to suppress lipid signal. This sequence is a fast gradient-echo with balanced gradient waveforms which generates contrast via a ratio of T2 toT1 weighting, with typical repetition and echo times of approximately 3.88ms and 1.54ms, respectively. The probe entry is planned by measuring distance from skin to target lesion and angle of entry. For image-guided probe placement, the trajectory is monitored by a real-time bssFP sequence, BEAT on the Siemens platform (TR: 922ms, TE: 2.32 ms). At this point, an image-guided biopsy of the tumor may be performed. To prepare for freezing, hydrodissection may also be performed to insulate and move nearby bowel. If bowel droops near the treatment zone during the procedure, hydrodissection may be applied between freeze/thaw cycles.

Monitoring begins when the probes are successfully localized and freezing is initiated. Multi-planar 2D mages are acquired every 3 minutes during the freeze cycle using either a half-Fourier acquired single shot sequence (HASTE; TR: 2000ms, TE: 83ms) or bssFP. The single shot sequence is employed to reduce artifacts caused by the multiple (n<5) cryo probes. Iceball edges are visualized as signal deficit due to long spin-lattice and very short spin-spin relaxation times of ice and are monitored to aid in assessing tumor coverage and avoid damaging nearby organs, particularly bowel [10]. The signal deficit caused by the iceball obscures the target tissue and tumor, which complicates quantification of the tumor coverage. Once the target iceball size has been reached, the tissue is thawed. Typically, two cycles of freezing and thawing are administered, however repeating the cycle depends on patient tolerance.

In the final step, after the second thaw, contrast is administered and uptake is monitored by a T1 weighted pre-contrast image, a T1-weighted dynamic sequence with four phases (3D Volumetric Interpolated Breath-hold sequence on Siemens platform; TR: 5.98ms, TE:

2.68ms), and a T1-weighted post-contrast image. The non-enhancing region within the organ is assumed to correlate with a lack of perfusion, verifying that the treated tissue no longer has functioning vasculature.

Each series may be acquired with a different resolution, contrast mechanism, or orientation as depicted in Figure 6-8. Even after applying isocenter matching and volume resampling, misalignments are still present between the planning and monitoring data sets, illustrated in Figure 4. Image alignment, or registration, can be applied in order to 'normalize' these variables and to make meaningful measurements across several data sets. Automated real-time image registration, which is a specific aim of this project, will be applied in step (2) to monitor the iceball for tumor coverage and to quantify and model the resulting edges of tissue necrosis. An example of the visualization of iceball and modeled perfusion loss is shown in Figure 5.
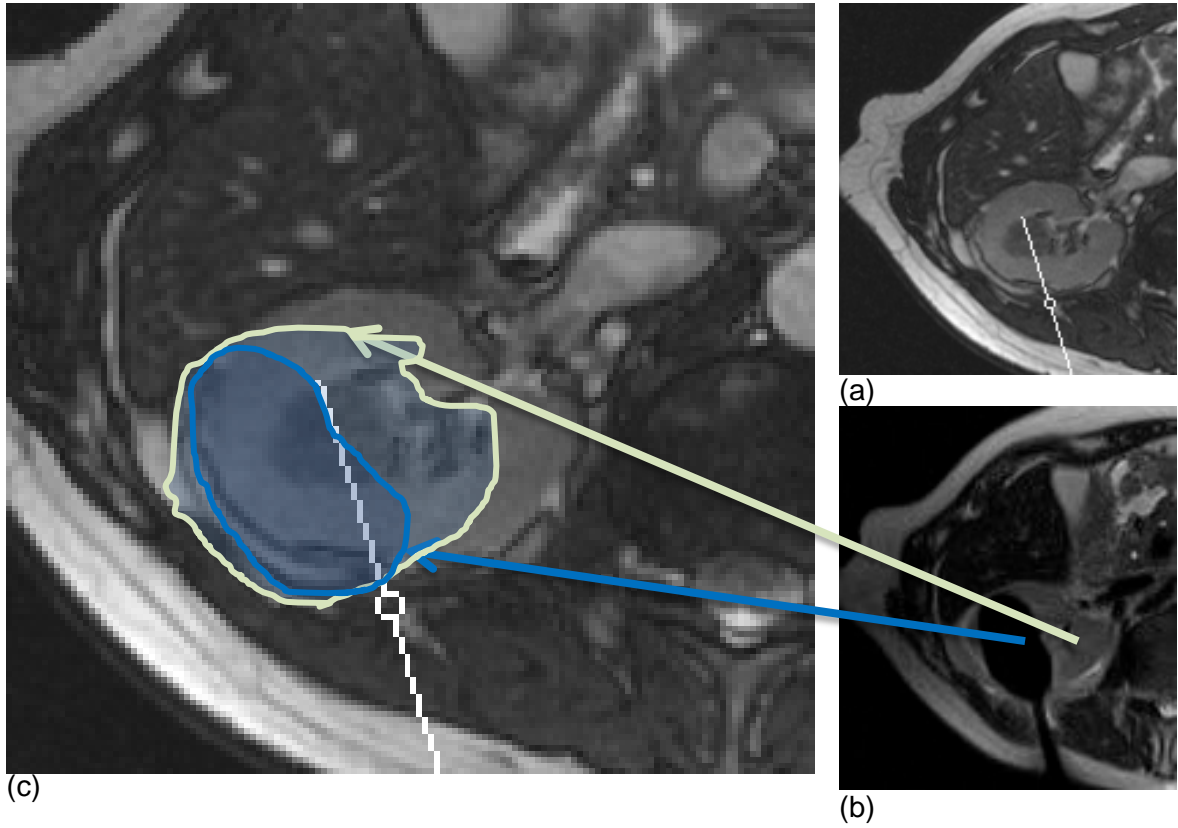
Figure 4: Example of 11.2 mm misalignment between planning and monitoring acquisitions on cropped images from (a) bssFP planning acquisition, axial slice, (b) ssFSE monitoring acquisition, axial slice, and (c) bssFP planning acquisition displaying the misaligned outline of the kidney on the monitoring acquisition
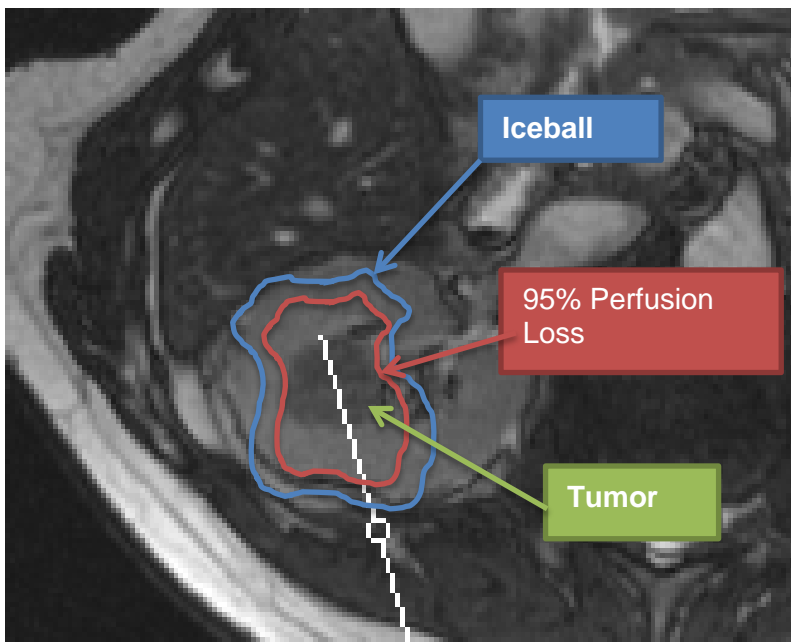
Figure 5: Illustration of final desired display, upon success of this project, including iceball contour and 95% perfusion loss likelihood overlaid on planning image
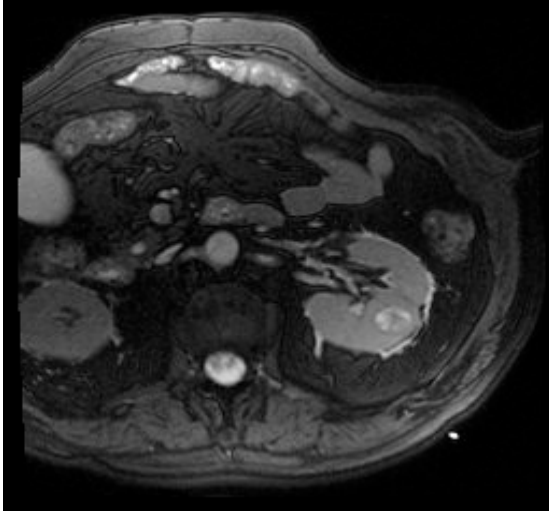
Figure 6: Planning/Lesion Identification Image (axial trueFISP with fat suppression, TR = 3.71 ms, TE = 1.47 ms, 256x256 FOV = 30x30cm)
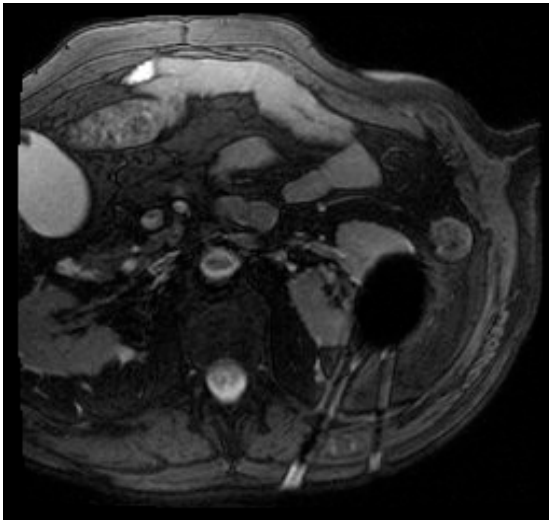
Figure 7: Iceball Monitoring Image (axial trueFISP with fat suppression, TR = 3.71 ms, TE = 1.47 ms, 256x256 FOV = 30x30cm)
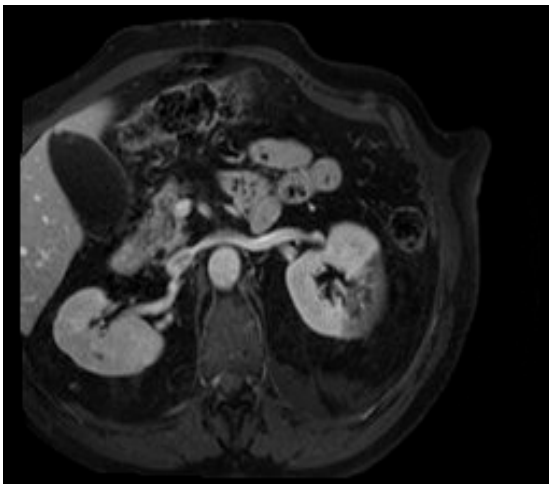
Figure 8: Evaluation/Post-procedural Image (axial T1+C with fat suppression, TR = 170 ms, TE = 4.76 ms, 256x192, FOV = 28.5x38.0cm)

All images courtesy of Dr. Kamran Ahrar, Interventional Radiology, The University of Texas MD Anderson Cancer Center

3 Techniques in Image Registration and Segmentation

Image registration is a technique that aligns a moving image series to a standard or reference image series. For the purposes of this project, it is also necessary to delineate the organ of interest (the kidney, in this case), the iceball, and the region of necrosis from the rest of the body. Delineating regions or organs in an image is termed 'image segmentation.' Through image segmentation and registration, we can align the regions of interest to a shared coordinate system so that each image can be quantitatively compared to another image from a different data set.

The problems of automated image registration and segmentation in medical imaging are long-standing issues that persist in areas such as fMRI, monitoring during image-guided procedures, and retrospective assessment of therapy response. Software packages exist which are dedicated to registration or segmentation as well as combined packages that handle both problems. Each specific aim will require separate approaches to tackling image registration and segmentation. For the quantification and modeling of perfusion loss in SA1, a highly accurate approach is needed for registration and segmentation, regardless of the time or user-interaction involved. For clinical visualization and feedback in SA2, speed and automation will determine the chosen methods for registration and segmentation. In both aims, the registration problem is complicated by missing information due to the iceball signal deficit.

3.1 Measures for Image Registration and Segmentation

To measure the success of the proposed registration algorithm, the Hausdorff distance and Dice Similarity Coefficients will be used to measure the remaining degree of misalignment between the two images.

3.1.1 Hausdorff distance (an absolute measure)

For rigid motions, the Hausdorff distance can be used as an absolute measure of the distance between a set of points, R, in the reference image and points in the moving

13

image, *M*. For each image, the Hausdorff distance represents the maximum Euclidean distance between reference and moving sets, *R* and *M*, and is determined by finding the maximum of the distance transforms, *h(R,M)* and *h(M,R)*.

$$H(R, M) = \max\{h(R, M), h(M, R)\}$$

$$h(R, M) = \max(Distance\ Transform from\ R\ to\ M)$$

Pseudo code of the Hausdorff distance algorithm is outlined below.

h(M,R)	h(R,M)
For i = 1:number of points of R	**For** i = 1:number of points of M
For j = 1:number of points of M	**For** j = 1:number of points of R
List = distance(R_i , M_j)	List = distance(M_i , R_j)
end	**end**
MinimumList = minimum(List)	MinimumList = minimum(List)
end	**end**
h(R,M) = maximum(MinimumList)	h(M,R) = maximum(MinimumList)

HD = maximum(h(R,M), h(M,R))

According to Huttenlocher, et al, the Hausdorff distance can also be used to compare portions of shapes. This 'partial' Hausdorff distance is calculated by ranking each point of the partial data (the moving image), *M*, by the distance to the nearest point of the complete reference, *R* [11]. Each non-zero point of *M* is assigned a ranking with respect to its distance from *R*, as opposed to calculating a single global maximum.

$$h_k(M, R) = k^{th} \min \big\| R(i, j) - M(i, j) \big\|, where\ k\ is\ the\ assigned\ rank$$

Ranked Hausdorff distances can indicate outliers to be ignored and can identify a mode distance between the points that is more descriptive than the maximum value.

3.1.2 Dice Similarity Coefficient (a relative measure)

The Dice Similarity Coefficient acts as a measure of inclusion between two sets. This similarity coefficient ranges from zero to unity and describes the extent to which one object overlaps another. From this perspective, the DSC can be used as a registration metric, where the DSC would be maximum when all points in the moving image, *M*, are encompassed by the points in the reference image, *R*. The Dice Similarity Coefficient is defined as:

$$DSC = \frac{2 * |R \cap M|}{|R| + |M|}$$

For application to binary vectors, the DSC becomes:

$$DSC_{binary} = \frac{2|R \cdot M|}{|R|^2 + |M|^2}$$

Figure 10 shows two test objects with a DSC of 32%, indicating that the shared number of pixels between the two objects comprises 32% of the total number of pixels of a single object. A DSC value of >70% corresponds to acceptable registration and DSC >75% is considered excellent agreement between objects [12].

The Dice Similarity Coefficient is limited as a metric for evaluating registration of a partial object to a full object. The area of the partial object could be encompassed by the whole object without actually being registered as illustrated in Figure 9, where successful registration would fit the partial piece to the top curve of the kidney mask. Using DSC and Hausdorff distance in combination can overcome this limitation and give more information about the registration results.

A successful approach to fast registration for this perioperative visualization tool will minimized the Hausdorff distance to below 3.3 mm while maximizing the DSC above at least 70%.
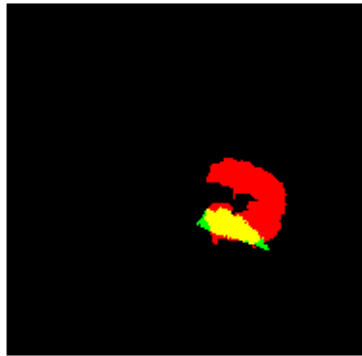
Figure 9: Illustration of High-Valued DSC with Erroneous Registration; the moving image (green piece) overlaps well with the reference image (red piece), however these images are not actually registered
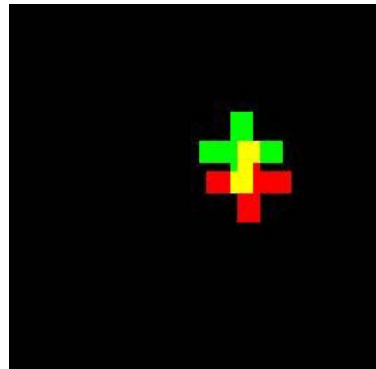
Figure 10: Illustration of Dice Similarity Coefficient of 32%; red =reference image, green = moving image, yellow = overlap

3.2   Image Registration

Image registration alters an image spatially so that it aligns with a reference image. This spatial altering can correct for rigid transformations (rotation, translation), affine transformations (rotation, translation, shearing), and deformations. The necessary spatial transformation can be defined by user-defined (interactive) or automated means. Typically, image registration can be summarized in the following steps:

- Compare the reference and a moving image by features or histograms

- Calculate a transformation matrix that optimizes the chosen registration metric

- Apply the transformation to the moving image

- Interpolate the moving image to the reference image coordinate system

16

From the literature, several registration methods were considered for use with this project. Both specific aims require a registration approach which can be generalized for data sets with varying contrast mechanisms and is robust to missing information (i.e., iceball-obscured kidney). In SA1, accuracy and gold standard methods are preferred to prepare data for statistical correlation and model creation. In SA2, the perioperative visualization is limited by time, so a quick registration approach is preferred. The summary and comparison of investigated potential registration methods is shown in Table 1, where gold-standard manual landmark registration was chosen for SA1 and the quick phase correlation performed using Fourier-transformed data was chosen for SA2.

Table 1: Summary of Described Registration Methods

Method	Multi-Contrast?	Handles Missing Information?	Accurate?	Fast (< 3 min)?
Feature Matching with Iterative Closest Point [13]	★			
Manual Landmark Matching [14] *SA1	★	★	★	
Area Methods with Normalized Mutual Information [13]	★	★	★	☆
Phase Correlation in the Fourier Domain [15] *SA2	★	★	☆	★

3.2.1 Interactive- Fiducial Based Methods

Fiducial-based registration methods require a set of user-defined points for each pair of reference/moving images. These points correspond to visual landmarks that are shared between the images. The points are matched pairwise across the two image stacks and can either be inherent to the image (i.e., patient markers) or can be chosen after image

acquisition by an expert. The transformation matrix describes the spatial shifts which minimize the mean squared distance between corresponding points in the images [13]. This method can achieve high accuracy since manual choice of the fiducial points avoids complications of missing information, segmentation, and computer vision. However, without consistent patient markers, fiducial-based registration is not ideal for clinical applications because choosing the fiducial points requires a significant amount of time and training. This highly interactive approach was used in SA1, for preparation of the images prior to correlating iceball edges and non-perfusion likelihood.

3.2.1.1 Landmark-Based Registration

Landmark-based registration is type of highly interactive fiducial point registration that can be applied to user-defined points or extended to user-defined regions which correspond pair-wise between the image stacks to be registered. Landmark-based registration is appropriate for the data in this retrospective study because it does not require pre-existing patient markers and can be used to generate a highly accurate, local rigid registration of the kidneys. Landmark-based registration available through several software platforms and the chosen platform, amira, is described below.

The amira software is a commercially available user-interactive system for visualizing data. The software was developed through the scientific visualization group at Zuse Institute Berlin and focused on display and analysis of volumetric data via 3D polygonal models [14]. The basic package includes modules for image segmentation, landmark editing, and several rigid and deformable registration options. The data type compatibility is a major advantage of amira; the package can handle both DICOM and MATLAB file types, which is preferable when using MATLAB scripts for automated measurement.

The LandmarkWarp module in amira allows the user to define corresponding landmark points between two sets of volume data. The moving image is then registered to the

reference image using a rigid or elastic transformation which minimizes the distance between the corresponding landmark points. The outputs of the LandmarkWarp are the registered moving image and the applied transformation matrix. After the registration step, the volumes can be visually inspected to confirm successful registration.

3.2.2 Automated Pixel Intensity Correlation

One approach to automating image registration relies on comparing the pixel intensity values between images. This approach seeks to maximize the normalized cross-correlation of the pixel values between the reference and moving images. The advantages of using cross-correlation as a metric are that it is easy to implement and can be adapted to run in real-time. Cross-correlation of the pixel values relies on superposition, so the moving image undergoes incremental spatial transformations until the normalized cross-correlation approaches unity. This cross-correlation method is only appropriate for images that have been acquired using the same contrast mechanism; therefore the application of intensity-based registration techniques is limited to single-modality and single-contrast data sets, such as CT. Furthermore, the normalized cross-correlation is not robust to missing information. Intensity correlation and modified intensity correlation methods are discussed below.

3.2.2.1 Modified Intensity Correlation with Histogram Classification

The algorithm for modified intensity correlation begins with a classification step, searching for groups of pixels with uniform intensity in each image. The assumption is that an organ or the same section of some organ will have relatively uniform intensity values which can be used to match the areas of reference and moving images. The algorithm projects the gray-value classification to the moving image, and then iteratively applies transformational changes in an attempt to minimize the standard deviation of the gray values in each class [16]. The error function to be minimized is:

$$error = \sum_{c=1}^{256} \sum_{v=1}^{n_c} (g_v - \overline{g_c})^2$$

Where g_v is gray level of the moving image in voxel *v*, and g_c is the mean value of all moving gray values in the class, *c.*

The final product is an output file that defines the transformation matrix that minimizes this error function, using a typical maximum of 50 iterations. The transformation matrix can be based on one of several models using 6, 9, or 12 degrees of freedom. The registration algorithm was reported to execute in approximately 1 second for a 256x256 2D image on a CPU clocked at 250 MHz; for a more modern 3.2 GHz processor, the calculations should take less than 0.1 seconds for a 256x256 2D image [17]. Modified intensity correlation with histogram classification would provide very fast image registration solutions even for larger 3D data sets, making the registration algorithm appropriate for clinical use.

Automated Image Registration (AIR) is an automated image registration package written in C and developed at UCLA that uses a modified pixel intensity correlation method [17]. This registration package has been extensively validated by the authors and their collaborators [16,17].The latest *AIR* package, v5.3.0 released in 2011, is available at http://bishopw.loni.ucla.edu/air5/. *AIR* has been designed specifically for registration of brain data sets and can be applied to data series across multiple modalities (e.g., MRI-MRI or PET-MRI). The native image data type is ANALYZE and *AIR* offers a header-creation program to convert raw image data to ANALYZE. The *AIR* package does not include a graphical user interface or any segmentation options; however the registration algorithm can be linked with other programs which provide a GUI.

Limitations of Modified Intensity Correlation with Histogram Classification

Although the registration algorithm itself is automated, the brain images need to undergo some pre-processing to increase the accuracy of the registration. It is recommended by the author that the user remove the scalp, dura, and skull from the image, leaving only the brain matter to be registered. Furthermore, because the registration algorithm is dependent on the intensity values within the image, the signal and contrast levels will have an impact on registration accuracy. For our application, i.e., monitoring an iceball during cryoablation, we must consider how the algorithm will respond to only partially visible kidney. According to the author, regions of signal deficit within the organ of interest will cause significant registration errors. *AIR* has been applied successfully for fast registration of brain data; however, this algorithm lacks robustness to missing information and is not appropriate for use in the cryoablation procedure.

3.2.3 Iterative Closest Point Registration

The iterative closest point algorithm is widely used in medical image registration and is appropriate for multi-modality data sets. The objective of iterative closest point is to minimize the distance between two sets of points defined from 2D or 3D surface meshes. The time of computation is dependent on the number of input points.

The iterative closest point registration requires a good initial estimate of the transformation in order to be successful, without which the iterations may converge to some erroneous local minimum. A number of methods have been devised for automated initialization of the closest point algorithm to avoid lengthy searches. Two popular initialization schemes are matching bitangent curve pairs – curves sharing the same tangent plane – for rigid and affine transformations [18] and matching invariant features, which requires image acquisitions from at least two different views to identify features which are invariant to motion[19]. Due to much iteration, ICP methods can be computationally intensive. ICP is

also quite sensitive to missing information, since curve matching algorithms are likely to

fail if the edge of an object of interest is not continuous.

3.2.4 Automated Registration using Normalized Mutual Information

One of the leading intensity-independent techniques in registering whole images is an

area based registration using mutual information as a similarity metric. The mutual

information describes the statistical dependency of one image on another. Mutual

information is expressed using the Shannon entropy of each image, *H(I). P(I)* is the

probability distribution of the intensity values of an image, determined by its histogram.

Equation 5: Mutual Information between Image X and Image Y

$$MI(I_1, I_2) = H(I_2) - H(I_2|I_1), where\ H(I_1) = -E_{I_1}(\log(P(I_1)))$$

The moving image will be transformed randomly and incrementally in an attempt to

maximize the mutual information between itself and the reference image. This expression

of mutual information is still sensitive to field of view and volume overlap of the images,

reducing the robustness of MI for registering partial data. Normalized mutual information

has been proposed to improve robustness to missing information in the images[20].

Normalized entropy considers the sum of the Shannon entropies of the two images

normalized by their mutual information. Successful registration is achieved when NMI is

minimized.

Equation 6: Normalized Mutual Information for Intensity Independence

$$NMI = \frac{H(I_1) + H(I_2)}{MI(I_1, I_2)}$$

Modern optimization schemes used with NMI employ multi-resolution approaches to

image registration for improved efficiency [13]. Registration methods using NMI are

typically robust however, for large volume data sets, calculating NMI is computationally

intensive. During optimization, NMI must be reevaluated for each perturbation of the moving image, which can contribute significantly to computation time.

3.2.4.1 Mutual Information-based Approaches for Rigid and Deformable Registration

Two popular techniques are often used when optimizing mutual information: the 'Demon' optical flow for deformable registration and a multi-resolution pyramid scheme to increase efficiency. The Demon approach applies optical-flow techniques for more fluid-like deformations; the optical flow approach typically optimizes similarity metrics of either mean square intensity difference in local regions or mutual information [21]. The multi-resolution module achieves registration through maximizing the mutual information between the two images and assessing the mutual information from different resolution steps. Multiresolution typically requires an initial guess as to the transformation parameters [13]. For either of these techniques, the registration for a 256x256 2D image can be calculated in about 1 second [21]. The algorithms would only be appropriate to register rather small data sets, which would ultimately limit the accuracy of the registration and resulting visualizations. Both approaches are available through 3D Slicer (http://www.slicer.org/), called BRAINSDemonWarp and Robust MultiResolution. BRAINSDemonWarp

3.2.5 Automated Phase Correlation and the Fourier-Mellin Transform

The phase correlation technique is an analytical and intensity-independent approach to image registration that takes advantage of the Fourier Shift Theorem. The cross-correlation of the two Fourier spectra is used to calculate the phase shift between the two images, which is then converted to spatial shifts in each dimension.

Intensity-independence results from the linearity property of the Fourier transform. The signal from one reference pixel is $i_{ref}(x,y)$ and the signal from any other pixel would

simply be a scalar multiple of the reference signal with the addition of a constant: $\mathbf{a}*$

$i_{ref}(x, y)\mathbf{b}$. By linearity, the Fourier transform of any pixel becomes:

$$\mathbf{a} * i_{ref}(x, y) + \mathbf{b} \overset{\mathcal{F}}{\leftrightarrow} \mathbf{a} * I_{ref}(\xi, \eta)$$

The Fourier transforms of $\mathbf{a} * i_{ref}(x, y)$ and $\mathbf{a} * i_{ref}(x, y) + \mathbf{b}$ are equivalent since the

functions only differ by a constant, $\mathbf{b}$. Intensity dependence can be eliminated by

normalizing the Fourier spectra of each image.

Phase Correlation: A Translation Solver
To solve for phase shifts, and therefore spatial shifts, the normalized Fourier spectra are

cross correlated. The Fourier Shift Theorem states that a translational shift in the spatial

domain corresponds to a phase shift in the frequency domain.

$$f(t - \tau) \overset{\mathcal{F}}{\leftrightarrow} e^{-i\omega\tau} F(\omega)$$

The moving image is defined as the reference image that is displaced by (x_0, y_0).

$Reference\ image: i_{ref}(x, y) \overset{\mathcal{F}}{\leftrightarrow} I_{ref}(\xi, \eta)$

$Moving\ image: i_{moving}(x, y) = i_{ref}(x - x_0, y - y_0) \overset{\mathcal{F}}{\leftrightarrow} I_{moving}(\xi, \eta) = e^{-i2\pi(\xi x_0 + \eta y_0)} I_{ref}(\xi, \eta)$

The translational displacement of the moving image can be solved for analytically by

calculating the correlation, or cross-power spectrum, of the reference and moving Fourier

transforms [15]. In Equation 9, we resolve a delta function by applying the Fourier

transform to the cross-power spectrum, where the horizontal and vertical coordinates of

the delta peak correspond to the translation shifts in x and y. This method can easily be

extended to three dimensions.

$$e^{i2*\pi(\alpha x + \beta y)} = \frac{I_{ref} * conj(I_{moving})}{\left|\left(I_{ref} * conj(I_{moving})\right)\right|}$$

$$\mathcal{F}\left(e^{i2*\pi(\alpha x + \beta y)}\right) = \delta(x_0, y_0)$$

$$Translation\ Transformation: \begin{bmatrix} 1 & 0 & x_0 \\ 0 & 1 & y_0 \\ 0 & 0 & 1 \end{bmatrix}$$

Fourier-Mellin Transform: A Rotation and Scale Solver

The phase correlation technique described above solves for translation shifts only. The

phase correlation can be adapted to solve for rotational and scaling shifts by applying

Fourier-Mellin Invariant Matching prior to calculating the phase correlation. Rotations in

image space result in identical rotations of the data of the Fourier transform. Fourier-Mellin

Invariant Matching requires transforming the magnitude of the Fourier transform to log-

polar coordinates prior to applying a second Fourier transform. The switch to log-polar

coordinates transforms the typical circular representation of k-space to a flat

representation which allows for correlation of two Fourier transforms.

$$Fourier\ Transform: i_{ref}(x, y) \overset{\mathcal{F}}{\leftrightarrow} I_{ref}(\xi, \eta)$$

$$Log - Polar\ Transform: \left|I_{ref}(\xi, \eta)\right| \overset{log-polar}{\Longleftrightarrow} I_{\log polar}(e^{\rho}, \theta)$$

$$Mellin\ Transform: \mathcal{F}\left[I_{\log polar}(e^{\rho}, \theta)\right] \overset{Mellin}{\longleftrightarrow} I_{Mellin}(u, v)$$

To solve for rotation and scale, the Fourier-Mellin transform is applied to the reference

and moving images and the correlation between these two matrices in calculated.

Through the Fourier-Mellin transformations, the translational shifts are ignored and the

rotational and scale shifts between the matrices are represented as horizontal and vertical

offsets, respectively [22]. Extending rotation to three dimensions would require performing

Fourier-Mellin transforms and phase correlation for each axis of rotation. One possible

approach would be to 'reslice' the volume in to three new volumes for axial, coronal, and sagittal orientations and then apply the rotation solver to each of these new volumes, resulting in scale and rotational shifts for each axis.

$$e^{i2*\pi(\alpha*\mathbf{u}+\beta*\mathbf{v})} = \frac{I_{ref,Mellin} * conj(I_{moving,Mellin})}{\left|\left(I_{ref,Melin} * conj(I_{moving,Mellin})\right)\right|}$$

$$\mathcal{F}\left(e^{i2*\pi(\alpha*\mathbf{u}+\beta*\mathbf{v})}\right) = \delta(\mathbf{u}, \mathbf{v})$$

$$(\mathbf{u}, \mathbf{v}) \rightarrow (scale, \theta_0)$$

$$Rotation\ Transformation\ @\ x - axis: \begin{bmatrix} scale * \cos(\theta_0) & -scale * \sin(\theta_0) & 0 \\ scale * \sin(\theta_0) & scale * \cos(\theta_0) & 0 \\ 0 & 0 & 1 \end{bmatrix}$$

The phase correlation method is advantageous because of its speed; there is no need for intensive iterations with this method, unlike the mutual information approach. However, because of the large number of spatial frequencies in a medical image, many spurious correlation peaks could be present in the correlation matrix. Some preprocessing will be necessary to prevent corrections that match the skin line rather than the kidney. A segmentation step could be implemented to identify the kidney within each image series before applying the phase correlation technique.

3.2.5.1 Registration Preparation: Removing Interfering Information
A possible registration preparation step would include segmentation of each image series, resulting in a label map or binary mask of a particular region or organ of interest. Highly accurate local registration can be achieved for specific organs of interest by registering the segmented binary masks rather than entire grayscale images. Here, we discuss segmentation techniques to be employed during the cryoablation monitoring before registration.

3.3   Image Segmentation

Image segmentation classifies different regions of an image based on user-identified or atlas-identified features within the image. The region of interest changes for each step during the procedure, therefore the segmentation technique needs to be flexible to accommodate not only various image acquisition parameters, but also new labels for additional regions of interest such as iceball and perfusion loss.

From the literature, multiple segmentation approaches were considered for use with this project. Both specific aims require segmentation methods which can be generalized for data sets with varying contrast mechanisms, are robust to weak boundaries in the image, and can identify multiple regions of interest. In SA1, accuracy and gold standard methods are preferred to prepare data for statistical correlation and model creation. In SA2, the perioperative visualization is limited by time, so a quick segmentation approach is preferred. The summary of potential segmentation methods is shown in Table 2: Summary of Described Segmentation Techniques, where gold-standard manual contouring was chosen for SA1 and the quick graph search using a random walker was chosen for SA2.

Table 2: Summary of Described Segmentation Techniques

Method	Multi-Contrast?	Handles Multiple ROIs?	Accurate?	Fast (< 3min)?
Graph Cuts with Shape Priors [23]	★			
Manual Contouring [14] *SA1	★	★	★	
Statistical Correlation [24]	★	★	★	☆
Graph Search via Random Walker [25] *SA2	★	★	☆	★

3.3.1 Interactive Contouring

Similar to registration, the most accurate method of segmentation is also the most user-interactive. The gold-standard of medical image segmentation is considered to be manual segmentation by a trained expert, also called contouring. Contouring is most commonly implemented by a radiologist or radiation oncologist for radiation treatment planning. The radiologist or oncologist will outline the target volume (or tumor) and the surrounding organs of interest on each image of the patient data set. Each unique organ or contour is assigned a single distinct value, resulting in a label map in which each region of interest has one homogenous color. Contouring is time-intensive and can be very accurate, but it is not appropriate for the time-restricted cryoablation procedure. This highly interactive approach was used in SA1, non-perfusion modeling, following registration of the images prior to measurement.

Manual segmentation is achieved using amira's LabelField module in the Segmentation Editor (http://www.vsg3d.com/amira/overview). There are several tools available to support manual segmentation including direct contouring, threshold-based contour, and region growing techniques based on a threshold or Gaussian filter. Threshold-based contouring is implemented by the user, where the upper and lower thresholds can be defined directly from adjusting the histogram display. Threshold region-growing segmentation can be interactively adjusting by applying general boundaries. Gaussian filter region-growing is tuned by changing the parameters of tolerance and width of the filter. The final segmentation labels for each region of interest can be output in DICOM or MATLAB format, which is very convenient for workflow in this project.

3.3.2 Semi-Automated Methods: Seed Placement with Random Walker Modeling

One semi-automated method prompts the user to choose pixels within an image and creates a label map based on the probability that a simulated randomly moving particle will reach those chosen pixels. This Random Walker algorithm for image segmentation is

based on a graph search which aims to solve the Dirichlet boundary problem [25]. The

image is decomposed into a graph of vertices and edges in which each edge is assigned

a weighting. This weighting represents the probability that a 'random walker' will cross that

particular edge and is dependent on intensity gradients within an image as well as

proximity to a seed. The node and edge weightings are analogous to resistors in a circuit

and the solution is obtained by solving the sparse linear system, following Kirchhoff's Law.

The algorithm is quite robust in the presence of noise or weak boundaries, however the

result is dependent on the number of 'seed pixels' chosen; the greater the number of seed

pixels, the easier the graph is to solve. The speed of this algorithm is appropriate for

clinical use.

3.3.2.1   Random Walker Software

The Random Walker segmentation algorithm was developed by Leo Grady and is in the

family of graph-cuts algorithms (http://cns.bu.edu/~lgrady/software.html), which

decomposes the pixels in the image to a mesh of weighted nodes and connecting edges.

The random walker relies on the user to define an arbitrary number of 'seed' pixels. The weights assigned to the nodes and edges depend on the proximity to a seed pixel as well as the local intensity gradients. In this way, the weights are analogous to resistances in a circuit, as illustrated in Figure 11. The algorithm results in a set of label maps that are derived from the probability of that a 'random walker' particle will arrive at the seed point, starting from some other pixel. The probabilities are binned into single-valued label maps. By definition, the number of label maps will be equal to the number of seed pixels chosen [25].
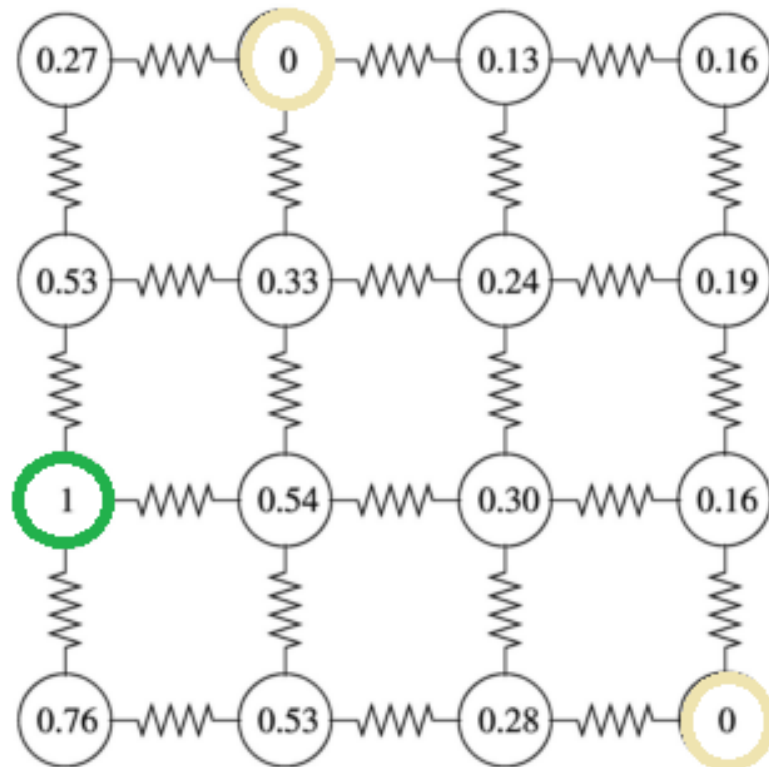

Figure 11: Random Walker Segmentation - Circuit Analysis [Grady, 2006]; the image to be segmented is decomposed into a series of nodes and edges, where weights are assigned that correspond to the probability that a random walker starting at some unlabeled node will reach the chosen seed node (green).

3.3.3 Semi-automated and Fully Automated Methods: Graph Cuts Segmentation with Shape Priors

The graph cut algorithm works similarly to the random walker in that the image is approached as a graph of nodes and edges and typically requires seed placement. In the case of graph cuts, the seed points are labeled as source/sink nodes and each path between the source and sink nodes is assessed for maximum flow with minimum boundary length. A known issue with this maximum flow/minimum boundary approach occurs in areas of low contrast, where the algorithm may result in only very small segmentations.

There are several semi-automated segmentation modules that are initialized by seed-point selection: Region growing, Grow Cut, and the Fast Marching modules. These techniques are generally sensitive to intensity gradients in the image and distance from the initial seed points. The final segmentation from each of these modules can be interactively adjusted by the user. The Fast Marching is reported to run in less than 1 minute for large data sets [26]. The Fast Marching algorithm may be acceptable for use during cryoablation, but 3D Slicer still lacks a fast intensity-independent registration module. Therefore, it is best to explore algorithms and programs other than 3D Slicer that can be implemented within MATLAB to aid in workflow.

A fully automated GC-prior method for segmentation of the iceball during cryotherapy has been proposed which relies on the maximum flow/minimum boundary algorithm [23]. Rather than interactively choosing source and sink nodes, the nodes (and approximate boundary) are defined from a prior shape – a model of the iceball. The model is a prolate spheroid with dimensions that were determined from experimental observation which required characterizing iceball size and shape created by probes of different diameters. Identification of each probe is performed manually before the segmentation begins and the centroid for the shape-prior is determined by observing the signal deficit of the iceball

during the first minute of freezing. This shape-prior method is very similar to atlas-based

segmentations that use approximate organ shapes to provide initial boundaries for

anatomical segmentation. After preparation and identification of probes, the segmentation

executes in approximately 15 seconds on a modern PC. This method not only includes

significant user-interaction, but also requires prior modeling based on probe diameter and

vendor.

3.3.4 Label Propagation for Segmentation from Prior Atlas

Segmentation propagation is an alternative to the curve-matching/boundary adjustment

step in atlas-based segmentation. Segmentation propagation can be initialized by a local

cross-correlation between the atlas and the normalized grayscale image [27]. The

segmentation propagation generates a pixel-wise probability map where is pixel is

assigned a likelihood that it belongs to a specific label or organ. Statistical segmentation

propagation is a little more lenient than curve-matching, making it more robust to

anatomical variability. However, segmentation propagation is still a multi-step process that

requires prior atlases and intensity-based correlations, so atlases would need to be

created for almost every MRI protocol (e.g., T1, T1 fat suppressed, T2, etc.). Although

segmentation propagation extends the flexibility of atlas matched segmentation, the

dependence on intensity-based correlation indicates that this method is not appropriate for

segmentation of cryoablation data.

EMSegmenter, available through *3D Slicer,* is an approach that allows the user to set up

pre-defined atlases that identify the tissues and organs of interest. These atlases may be

produced by manual contouring and are used as templates for automated segmentation

on new data, as long as that data has been acquired under the same imaging protocol.

Creating the prior atlases requires time and training and an individual atlas would need to

be created for each possible imaging protocol that is used during the procedure.

Furthermore, the prior atlas would be to be registered to the current image before

segmentation begins, resulting in increased computation time. Therefore, the prior-atlas

segmentation technique is not appropriate for our methods because it does not have the

flexibility required by the cryoablation procedure.

4   Materials and Methods

4.1   Specific Aim 1: Measuring Visualized Perfusion Loss and Modeling Perfusion Loss Likelihood from Iceball Edges

For the first specific aim, the emphasis is accuracy. Therefore, the registration and

segmentation techniques used to achieve this aim were gold-standard techniques

implemented using the amira package for image processing.

Four major steps were completed for data processing and analysis to compare the iceball

size and resulting perfusion loss region: manual registration and manual segmentation

trials were completed using amira, ground truth estimation from the segmentation trials

was completed via STAPLE, and automated statistical correlation between the iceball and

perfusion loss ground truth segmentations was executed via original MATLAB scripts. The

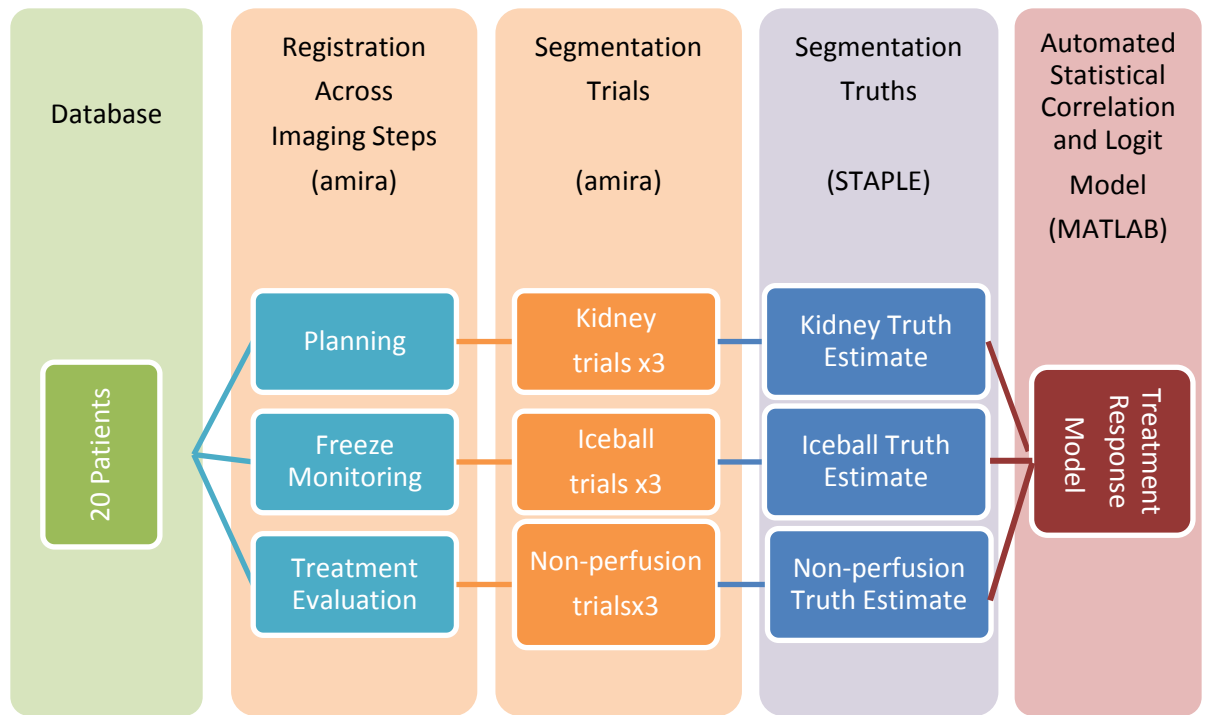workflow data processing is illustrated below in Figure 12.

Figure 12: Workflow for manual registration and segmentation trials, segmentation truth estimation, and statistical correlation and modeling

4.1.1 Materials for Measuring Visualized Perfusion Loss and Modeling Perfusion Loss Likelihood from Iceball Edges

4.1.1.1 Manual Registration and Segmentation via amira

The amira software is highly interactive system available through the Visualization Sciences Group (www.vsg3d.com/amira) and can accommodate many file formats, including DICOM and MATLAB, which is ideal for our MATLAB-heavy workflow. This software includes many modules and add-ons to perform higher level image processing, registration, and visual modeling and has been validated [14]. The relevant amira modules for this project were:

- Volume Resampling

- Rigid Registration via Manually-Identified Points

- Label Creation via Manual Segmentation

All manual registration and segmentation was performed in amira, followed by automated measurement and analysis via MATLAB.

4.1.1.2 Segmentation Ground-Truth Estimations via STAPLE

The problem of image segmentation is further complicated by the need to assess the accuracy or 'truth' of the segmentation. Manual segmentation by trained experts has historically served as the gold standard, however experts are not always available to segment large data sets and segmentations between multiple experts may differ significantly. In order to validate new segmentation techniques or compensate for variability among expert segmentations, the statistical STAPLE method can be applied to estimate a 'ground truth' or gold standard segmentation. From this estimated truth, we can assess the performance of the new automated technique or the experts themselves. The STAPLE algorithm is offered as a command-line based program with an optional GUI for visualization and is available at http://crl.med.harvard.edu/software/STAPLE/.

The STAPLE algorithm relies on an Expectation-Maximization scheme that determines a true 'hidden' segmentation from a group of prior segmentations. The method is entirely statistical; the final truth estimate is a voxel-wise probability map calculated from analyzing the prior segmentations [28]. A threshold can be applied to the probability map to generate a binary segmentation.

The Expectation step calculates an estimation of the complete log likelihood of the true segmentation based on the performance levels (θ in Equation 12) calculated from each prior segmentation. The performance levels are the true positive and true negative fractions.

Equation 12: Complete Log Likelihood Function

$$\ln L_c\{\theta\} = \ln f\left(D_{1:J}, T\middle|\theta\right)$$

$where\ \theta: perfomance\ levels\ of\ all\ segmenters; D: all\ J\ segmentations; T: truth$

This step calculates a truth probability map, *W*, from the prior segmentations which are weighted by their respective performance levels at iteration *k.* The performance level *θ* is decomposed into the true positive and true negative fractions, *p and q*, respectively, to prepare for the Maximization step.

$$Estimation\ of\ True\ Pixels: a(k) = f(T = 1) \prod_1^J f(D_j|T = 1) * p_j(k) * q_j(k)$$

$$Estimation\ of\ Not - True\ Pixels: b(k) = f(T = 0) \prod_1^J f(D_j|T = 0) * p_j(k) * q_j(k)$$

$$Estimation\ of\ True\ Segmentation: W(k - 1) = \frac{a(k - 1)}{a(k - 1) + b(k - 1)}$$

The Maximization steps focuses on maximizing the true positive and true negative fractions, which consequently maximizes the complete log likelihood of the truth estimate. To update the performance levels, the prior segmentations are compared to the truth probability map, *W*, from the Estimation step.

$$True\ Positive\ Fraction: p_j(k) = \frac{\sum_{1:J}(D_j = 1)W(k - 1)}{\sum W(k - 1)}$$

$$True\ Negative\ Fraction: q_j(k) = \frac{\sum_{1:J}(D_j = 0)(1 - W(k - 1))}{\sum(1 - W(k - 1))}$$

The iteration continues until the estimation of the true segmentation no longer changes, implying that the algorithm has converged upon a solution.

$$|W(k) - W(k - 1)| < 10^{-6}$$

4.1.1.3 Modeling Perfusion Loss Likelihood from Iceball Edges with Logistic Regression

Logistic regression, or the 'logit model', is in the family of generalized linear models. The logit model is used for categorical or binary data, for example, tissue is ablated/not ablated. Logit models are widely used in radiation biology to describe cell survival rates as a function of exposure to ionizing radiation. The underlying distribution for these cell survival models is the Poisson distribution and the model is constructed using the logit link function in Equation 16.

Equation 16: Logistic Regression Model

$$Probability(cell = dead | dose = d_1) = \frac{e^{\alpha + \beta * d_1}}{1 - e^{\alpha + \beta * d_1}},$$

Where α and β are regression coefficients that are typically determined using an iterative maximum likelihood estimation. In radiation dose response, the coefficients correspond to physical parameters: the α/β ratio indicates the 50% response (LD_{50}) and 1/ β is the slope of the dose response curve.

For this project, the logit model would describe the probability of perfusion loss (seeing a non-enhancing pixel) as a function of distance within the edge of the iceball, as illustrated in Figure 13. Using this model, the likelihood of perfusion loss in renal tissue can be reported at each distance within the iceball. Note that in the example curve, Figure 13, perfusion loss may not occur at the outer edges of the iceball. It has been shown that tissue must be exposed to temperatures of approximately 20˚C to cause perfusion loss and necrosis [1], however the outer edge of the iceball is typically closer to 0˚C.
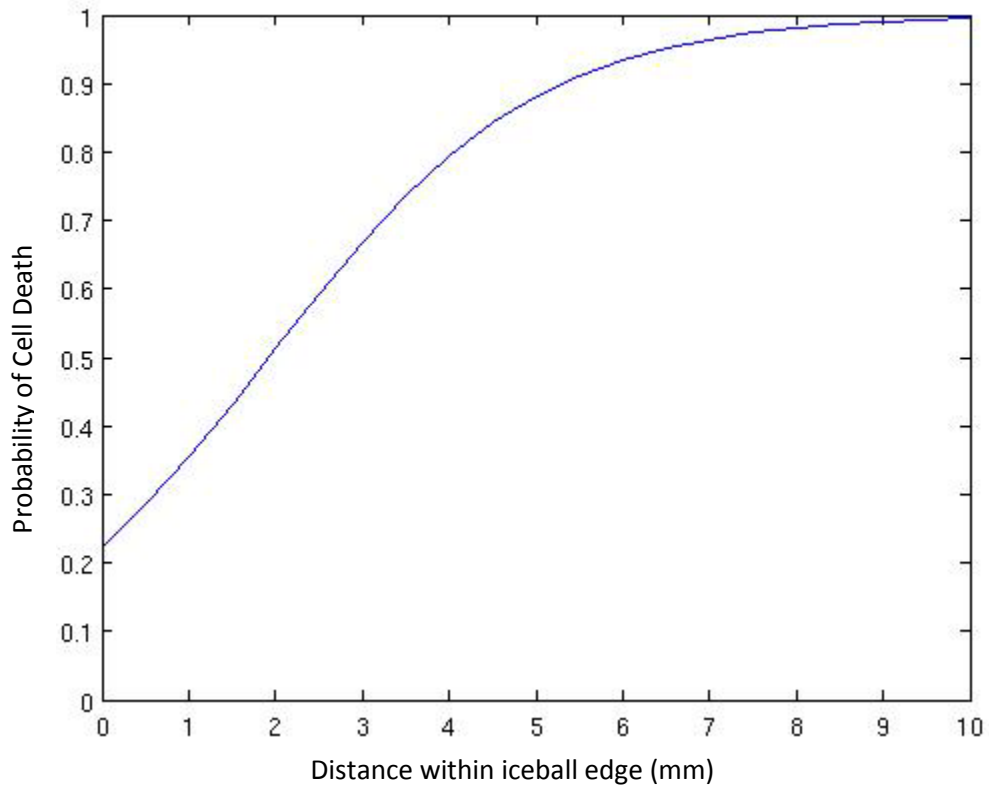
Figure 13: Example Survival Curve for Tumor Cells during Cryoablation, due to the non-uniform temperature of the iceball, perfusion loss is much less likely at the outer edge of the iceball, indicating that there exists an ineffective outer margin of the iceball that needs to be quantified and considered during treatment.

4.1.1.4 Limitations of Logistic Regression

In our case, the logistic regression model for tumor cell survival is generated solely from image data, which leads to two major limitations: 1) Cryoablation affects several abdominal tissues, including renal parenchyma, perirenal lipid, and less frequently, muscle. The perfusion rates differ among these tissues, resulting in a different response or different visualized margin in each tissue. It may be necessary to evaluate each tissue response separately. 2) The model does not consider any temperature distribution within the iceball. If the iceball does not have uniform sub-zero temperatures, the predicted region of perfusion loss would be inaccurate.

4.1.2 Methods for Measuring Visualized Perfusion Loss and Modeling Perfusion Loss Likelihood from Iceball Edges: Image Processing and Statistical Correlation

Manual Registration and Segmentation Trials in amira:

The goal of this registration was to align all three data sets – planning, iceball monitoring, and treatment evaluation (perfusion loss) and to segment the regions of interest in each set. Segmentation ground truth estimation requires at least 3 trials, so manual segmentation was repeated 3 times for each region of interest in each patient study.

Planning, iceball monitoring, and treatment evaluation series were loaded from a single patient study. Each series was resampled to 1mmx1mmx1mm pixel size. The iceball monitoring series was chose as 'reference,' so the transformations were applied only to the planning and treatment evaluation images. Registration of the three series was initiated by choosing control points. The control points were placed on corresponding anatomical landmarks common to the data sets (i.e., ureters, spinal processes, visible renal borders) in the neighborhood of the kidney. At least 5 control points were chosen for each set as illustrated in Figure 14. Notice that this registration is local and restricted to the kidney. This registration was not applied to perirenal adipose or nearby bowel, so measurements of perfusion loss were only made in renal parenchyma.

The transformation was calculated for both 'moving' series, i.e. planning and evaluation data, individually using an iterative-closest-point-based rigid registration algorithm provided in amira. The respective transformations were applied to the planning and treatment evaluation series. After registration, the series were cropped to identical pixel dimensions (very important for MATLAB measurements) and exported in the DICOM format.
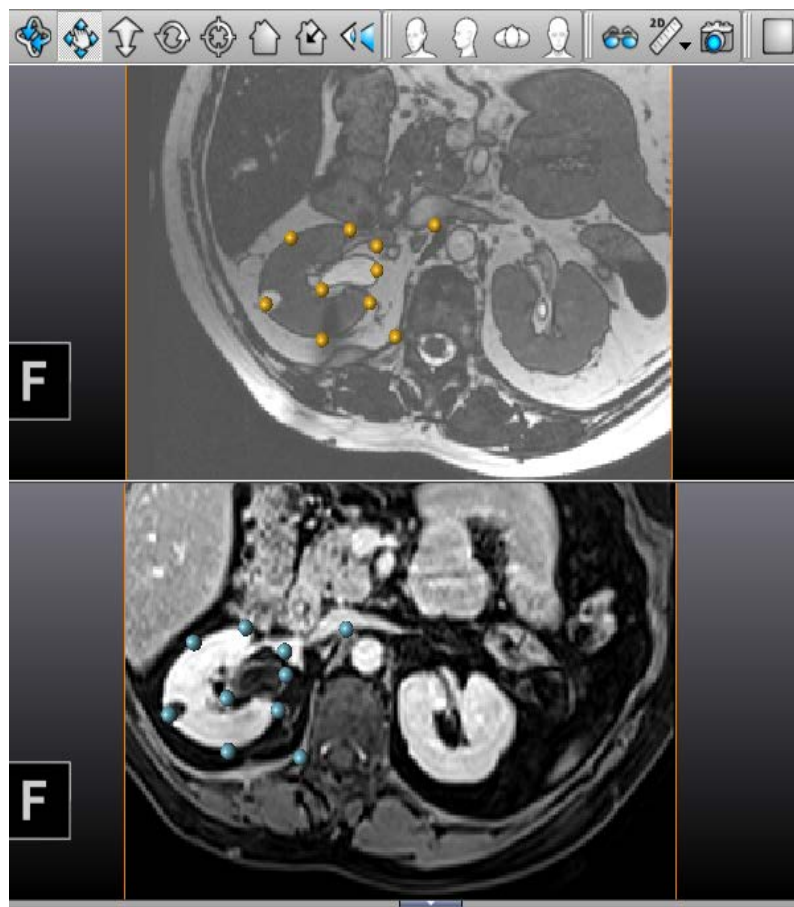

Figure 14: Step 3 - Manual Registration via Control Points in amira; top – monitoring image with landmark points (yellow); bottom – treatment evaluation image to be registered with corresponding landmark points (blue)

Label maps were created from manual segmentations of each slice. The region of interest for each series was:

    i.   Planning series: Kidney and Target Lesion, shown in Figure 15: Segmentation of registered image stacks in amira (a).

    ii.   Iceball series: frozen region indicated by total signal deficit (black pixels) illustrated in Figure 15: Segmentation of registered image stacks in amira (b)

    iii.   Treatment evaluation series: ablated low perfusion area in the kidney, defined as the lower signal region in the contrast-enhanced images illustrated in Figure 15: Segmentation of registered image stacks in amira (c).

Truth estimation requires at least three trials of a segmentation to achieve a good result; therefore, segmentations were repeated 3 times for each planning, iceball, and evaluation series.
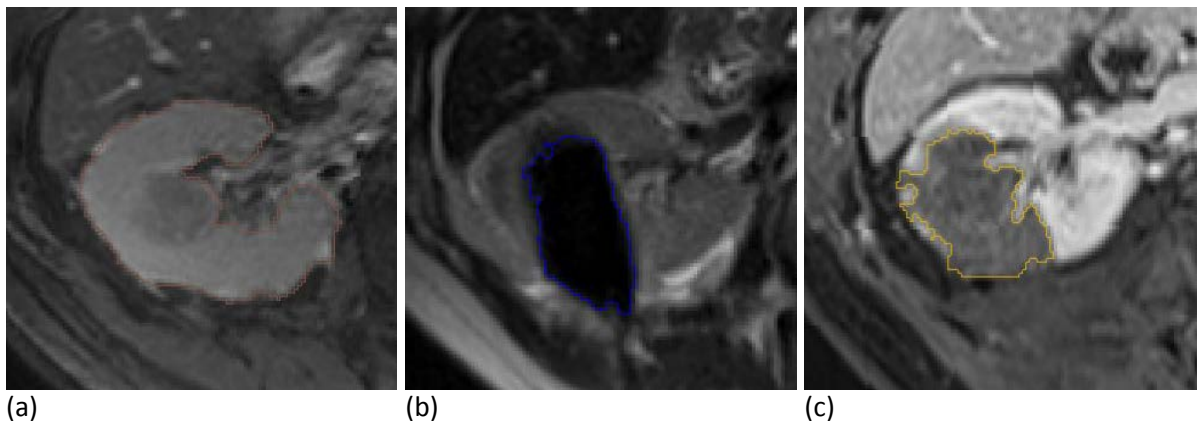

(a)   (b)   (c)

Figure 15: Segmentation of registered image stacks in amira; (a) Planning slice: kidney and tumor segmentation in orange contour; (b) Monitoring slice: iceball segmentation in blue contour; (c) Evaluation slice: perfusion loss segmentation in yellow contour

Segmentation Truth Estimation:

All label maps were converted from DICOM to NRRD volumes files for compatibility with STAPLE. To compute the 'true' segmentation, the three trials from each step are submitted to STAPLE, which returned a single NRRD file containing the estimated truth. Figure 16 is a Venn diagram which illustrates how each of the three segmentation trials can contribute to the final truth estimation.
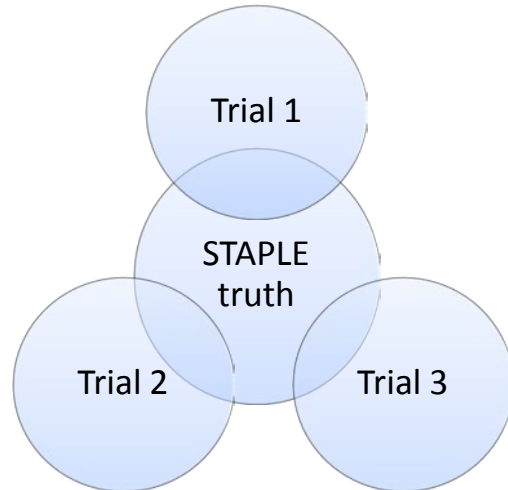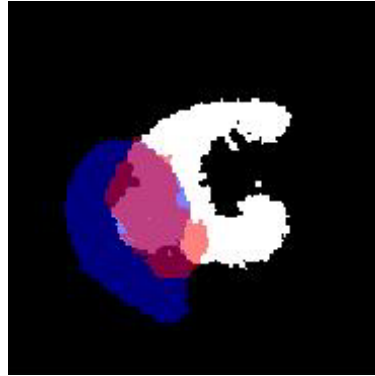
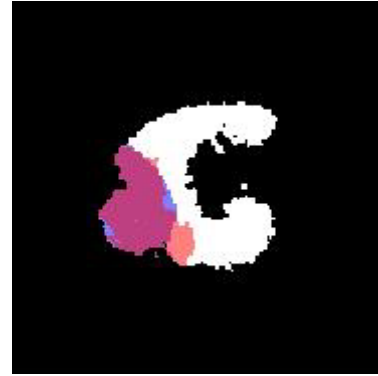*Automated Statistical Correlation and Modeling between Visualized Iceball and Perfusion Loss:*

The goal of this MATLAB script was to perform measurements on the iceball and perfusion loss segmentations and fit these measurements to a logit model. The 'true' segmentations for the kidney, iceball, and perfusion loss region were submitted to the in-house MATLAB functions for measurement.

Within MATLAB, measurements of the iceball and perfusion loss segmentations were made only in the renal parenchyma, not in the surrounding fat. The kidney label map was used as an inclusion mask such that only the parts of the iceball and perfusion loss area within the kidney boundaries were assessed. Automatic exclusion of iceball and perfusion loss outside the kidney boundaries is illustrated in Figure 18.
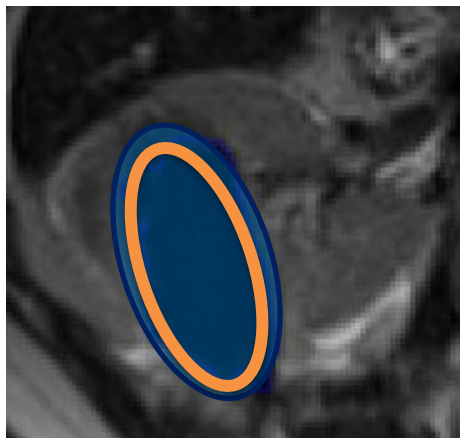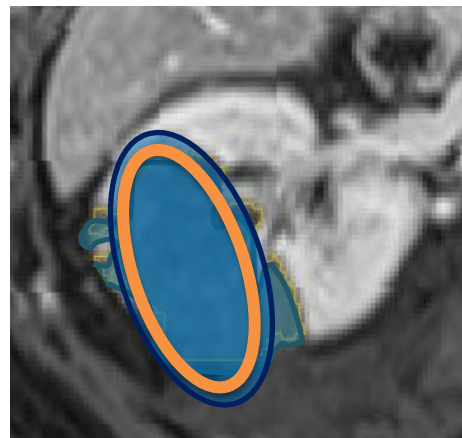
(a)   (b)

The ablation fraction was calculated by measuring the intersection between the iceball and the perfusion loss maps at 1mm increments inside and outside the iceball (shown in Figure 18). The 'direction' was defined as:

> a. Distance > 0 for perfusion loss edge within iceball edge
>
> b. Distance < 0 for perfusion loss edge extending outside iceball edge.

(a)   (b)

Measurements of perfusion loss fraction versus distance in iceball were submitted to an iterative generalized linear fit script with logit link function, available as `glmfit` in MATLAB. A sigmoid curve was created to display likelihood of tissue perfusion loss as a function of distance within the border of the iceball.

4.2 Specific Aim 2: Semi-Automated Perioperative Visualization of Target Coverage

Perioperative visualization provides information and feedback to the radiologist during the procedure. Therefore, appropriate methods must execute within a clinically relevant time period – in the 3 minutes between monitoring acquisitions for cryoablation. An analytical (immediate solution) method was therefore investigated in order to avoid iterative methods that could possibly introduce a lag due to intensive computation. All computation was performed using MATLAB in a Linux environment (GNOME with Intel® Xeon® CPU @ 2.40GHz). The general steps of the visualization tool, including segmentation preparation, are outlined below in Figure 19. First, the user defined the location of the planning and monitoring images, then the Random Walker algorithm for semi-automated segmentation was applied to generate segmentation masks of kidneys and iceball. The segmentation masks were then registered and the rigid transformations were saved and applied to the iceball segmentation mask. Finally, the perfusion loss model was applied to generate estimated likelihood of damage and contours of iceball position and damage likelihood were projected onto the planning image.
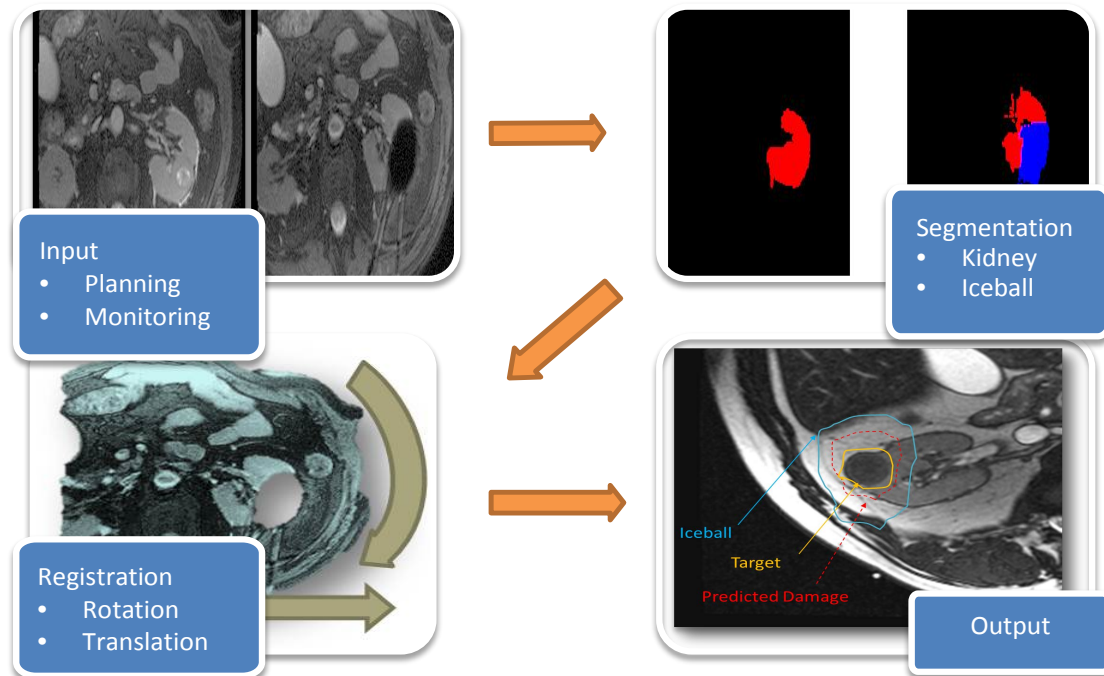
Figure 19: Illustration of general steps involved in perioperative visualization; (top left) user specifies series directory (top right) semi-automated random walker segmentation is applied to define kidneys; (bottom left) phase correlation registration solves for rotation and translation parameters; (bottom right) registered iceball position and likelihood of perfusion loss are displayed as contours on the initial planning image

4.2.1 Materials for Perioperative Visualization of Target Coverage

4.2.1.1 Fourier-Mellin Invariant Descriptors and Phase-Only Matched Filter for Rigid Registration

The phase correlation method for image registration was first proposed by Kuglin and Hines in 1975. The phase correlation method is effective because the displacement between two images can be determined by inspecting the phase of the cross power spectrum of the pair. The advantage of the phase correlation over the established cross correlation method is two-fold: 1) phase correlation is 'scene-independent;' it is not affected by intensity differences between the images; and 2) the peak of phase correlation (the solution) is typically sharp and only one pixel wide – thereby avoiding erroneous alternative solutions. Kuglin and Hines proposed a solution specifically for compensating for translational shifts, and the concept of phase correlation has been expanded to accommodate full rigid registration, including both rotational and translational shifts, for pixel and sub-pixel accuracy[29].

This registration problem is solved in two steps, by applying Fourier-Mellin Invariant matching to obtain shifts in rotation and scale, followed by the Phase-Only Matched Filter for shifts in translation. The Fourier-Mellin Invariant matching is so termed because this approach to the rotation and scaling solution is independent of any translational displacements. The Fourier-Mellin solution is derived from the correlation of the spectral magnitude of the log-polar Fourier transform of each image. The coordinates of the observed peak correspond to the rotation angle and scale factor between the two images. For the second step, we correlate the spectral phase of the Cartesian Fourier transform of each image. In this case, the coordinates of the correlation peak correspond to the horizontal and vertical shifts. An example of this two-step process is illustrated in Figure 20. The rotation and scale factors and translational shifts are housed in separate transformation matrices. This method can be used to achieve pixel-level accuracy and can be expanded to sub-pixel accuracy by capitalizing on zero-padding properties in the Fourier domain or by simple center-of-mass calculations from several correlation peaks [15,29].

4.2.1.2 Subpixel Transformation Calculation

Two subpixel registration methods are available which increase the accuracy of the phase correlation registration.

Center of Mass

The Center of Mass approach is a slight alteration of the original whole-pixel registration. Rather than search for the position of a single maximum peak within the phase correlation matrix, the Center of Mass technique takes a 5x5x5 pixel region centered around the maximum peak. To achieve the fractional transformation values, the center-of-mass is calculated for this 5x5x5 pixel region. This method can achieve transformation solutions whose resolution is not fundamentally limited while maintaining efficiency.

The Zero-Padding approach to subpixel registration takes advantage of the properties of the Fourier transform. Once the original size phase correlation is calculated, it is embedded into a larger matrix of zeros that is twice the size of the original. The large matrix can be scaled up to three, four, or more times the size of the original, depending on the desired resolution of the fractional transformation. The Fourier transform of the this zero-padded large matrix results in an interpolated transformation of the original phase correlation data with a higher effective resolution. Efficiency is sacrificed for improved resolution in the transformation solution due to the computation time when calculation fast Fourier transforms of very large matrices.

Log Polar Fourier Transform (Spectral Magnitude)

Log(rho)

theta

Phase of the Cartesian Fourier Transform

y

x

Spectral Cross Correlation:

$$e^{i2\pi(\alpha x + \beta y)} = \frac{FT(Image1) * conj(FT(Image2))}{|FT(Image1) * conj(FT(Image2))|}$$

$$R = \begin{pmatrix} \rho\cos(\theta) & \rho r\sin(\theta) & 0 \\ -\rho\sin(\theta) & \rho\cos(\theta) & 0 \\ 0 & 0 & 1 \end{pmatrix}$$

$$T = \begin{pmatrix} 1 & 0 & dx \\ 0 & 1 & dy \\ 0 & 0 & dz \end{pmatrix}$$
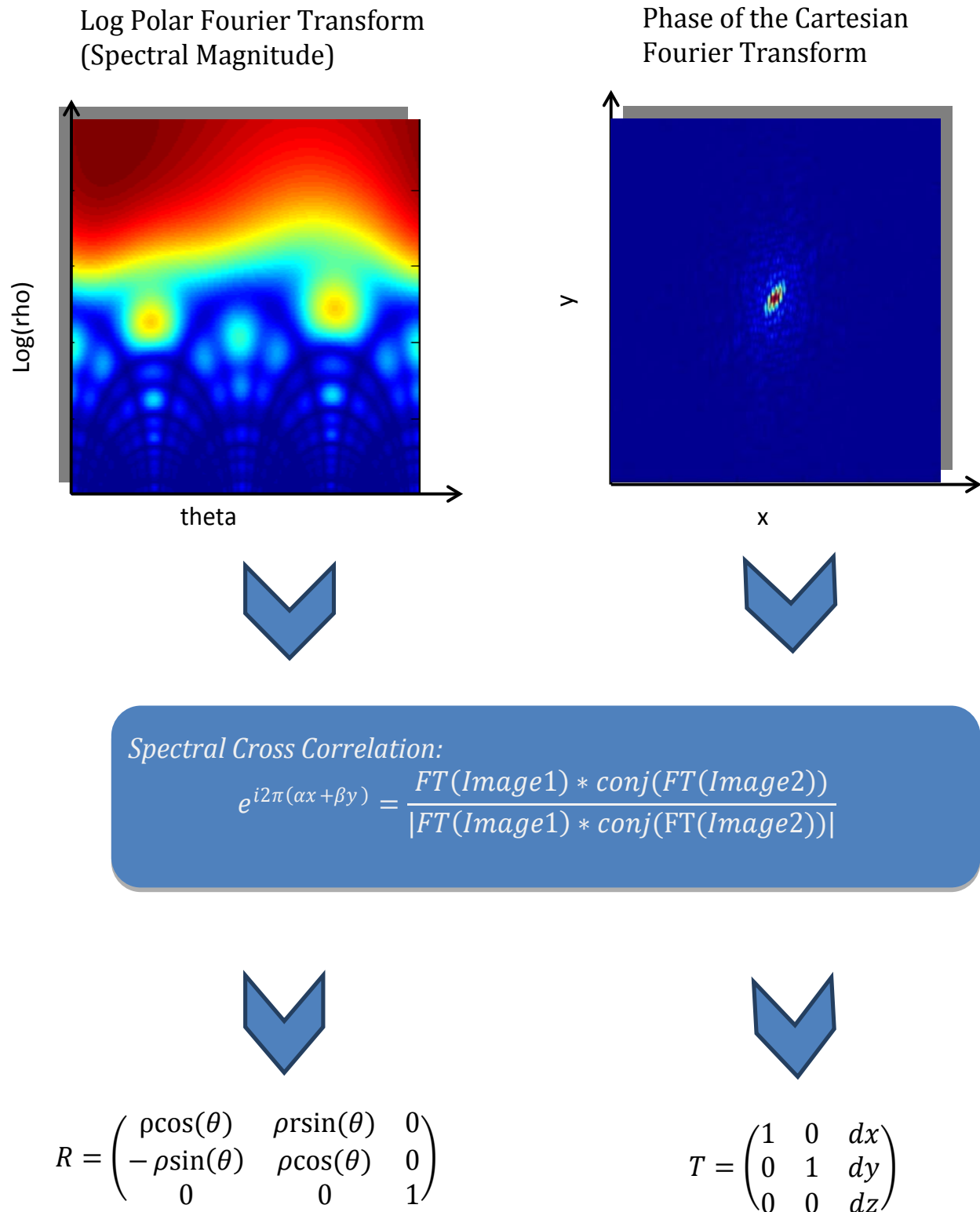
Figure 20: Phase Correlation Method for Rigid Registration (top left) Fourier Mellin image used for rotation solving (top right) spectral Fourier image for translation solving; (center) phase correlation peak is found from the correlation matrix of Fourier transformations; (bottom left) Fourier-Mellin correlation peak coordinates are transformed to rotation and scale parameters; (bottom right) spectral correlation peak coordinates are transformed to translation parameters.

Methods for Perioperative Visualization of Target Coverage

4.2.2.1   User-Defines Image Locations

The user chose the directories for planning images and iceball monitoring images. These

images were in DICOM format. The planning image was defined as the 'Reference' and

the monitoring image was 'Moving' (the images to which we will apply a transformation).

Using DICOM header information, the slices of each series were sorted by spatial

coordinates from the header. Both series were resampled to 1mmx1mmx1mm resolution

and adjusted (i.e., cropped or expanded) to identical dimensions.

4.2.2.2   Semi-Automated Segmentation

The semi-automated Random Walker Segmentation was initiated by the user choosing at

least 5 seed points on a particular slice of each series. The regions of interest for

segmentation were:

a.   Planning series: kidney including target lesion (label = 1)

b.   Iceball series: visible kidney (label = 1) and iceball signal deficit area (label = 2)

After the Random Walker runs, the user was prompted to accept or reject the

segmentation. If rejected, the user defines new seed points and the segmentation was run

again. If accepted, the seed points and label maps of all slice of each series are saved.

Figure 21 depicts the display of the original planning image with selected seed points and

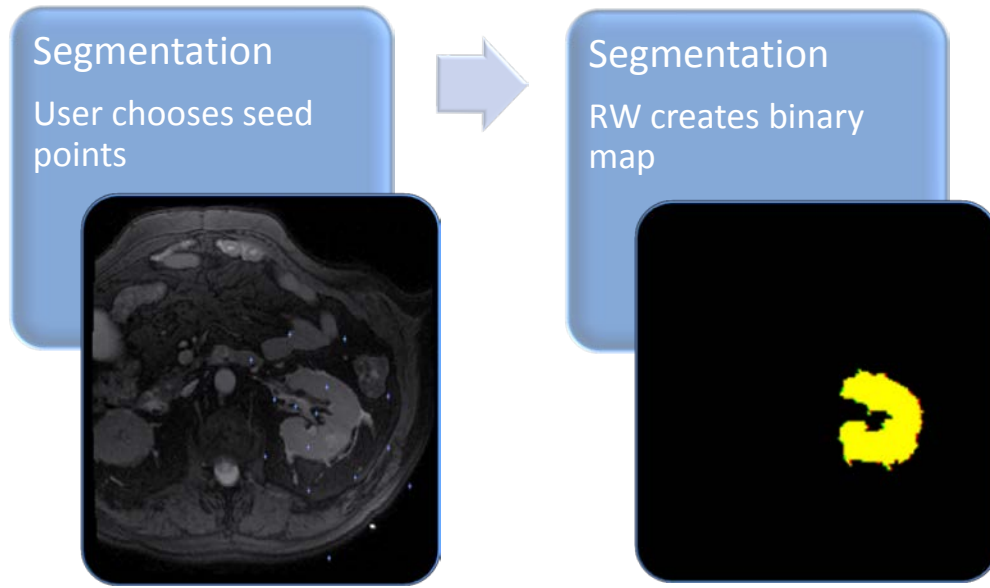the resulting segmentation mask of the kidney.

Figure 21: step 4 - Semi-Automated Segmentation by User-Defined Seed Points in MATLAB; (left) planning image with foreground and background seed points defined (right) resulting segmentation mask of kidney

The label map series from the segmentation and the original image stacks were then resampled to 1mmx1mmx1mm pixel size. The initial Hausdorff distance was measured between the planning and monitoring kidney edges (where label = 1 in both maps). Both binary series are then input to the registration algorithm. The initial Hausdorff distance was used to constrain the final transformation parameters by discarding any peaks in the solution that may appear outside the range of that initial HD.

4.2.2.3 Automated Registration via Fourier-Mellin Invariant Matching and Phase Correlation

The registration solves for first the rotation transformation, then the translation transformation:

Rotation Solver:

The Fourier Transform of the Reference and Moving images stacks was taken, slice-by-slice (in 2D) and the Fourier transforms are converted to log-polar coordinates. The log-polar Fourier transforms are cross-correlated, giving a 3D matrix in which each pixel value was the value of the correlation between the two images at that location. A constrained

search was executed to find the highest peak value within the constraints. Here, the search space would extend one Hausdorff distance from the center of the correlation matrix in each direction, ensuring that the resulting transformation will not increase the Hausdorff distance between the images.

To improve accuracy, the Center of Mass subpixel registration method was applied to calculate fractional transformation parameters. The coordinates of the maximum correlation (highest pixel value) are found: the first coordinate (rows) determines the scaling, the second coordinate (columns) determines the angle of rotation, and the third coordinate is not used. The rotation and scale shifts were applied in-plane. No rotation was applied along the slice direction unless large misalignments were still apparent.

Translation Solver:

The Fourier Transforms of the Reference and Moving images stacks were calculated. The Fourier transforms were cross-correlated, giving a 3D matrix in which each pixel value was the value of the correlation between the two images at that location. Again, the Center of Mass sub-pixel method was applied and a constrained search was executed.

The coordinates of the maximum correlation (highest pixel value) were found: the first coordinate (rows) determined the shift in x, the second coordinate (columns) determined the shift in y, and the third coordinate determined the shift in z (along the slice direction).The translational shifts were applied along all three dimensions. The rotation angle and scale factor were incorporated into one transformation matrix, and the x, y, and z translational shifts went into a separate transformation matrix. These transformations were sequentially applied to the iceball segmentation mask to register the iceball mask to the planning image.

4.2.2.4 Display of Iceball Position and Perfusion Loss Model

Finally, the registered iceball mask was projected onto the planning image in its accurate location. At this point, the volume of the iceball was automatically measured and tumor coverage was assessed visually by the interventional radiologist. The damage model from SA1 was incorporated to calculate probability of perfusion loss and display perfusion loss contours onto the planning image.

5 Results and Discussion

5.1 Specific Aim 1: Measuring Visualized Perfusion Loss and Modeling Perfusion Loss Likelihood from Iceball Edges

Twenty previous cryoablation cases were manually registered and segmented in amira for kidney in the planning images, low-signal iceball in the monitoring images, and low-signal perfusion loss in the evaluation images. Using MATLAB, the contour maps were processed and measured. The kidney map was used as an inclusion mask to identify the section of the iceball and perfusion loss that occurred within the kidney tissue. Only the iceball and perfusion loss within the kidney were considered for measurement. Average observed volumes for tumor, iceball and perfusion loss are listed in Table 3. For comparison, the total volumes of iceball and perfusion loss in all tissue for each case are displayed in Figure 22. Occasionally, visualized perfusion loss may extend far beyond the edges of the iceball, as indicated by the larger perfusion loss volume in case 19. For case 19 in particular, the spread of perfusion loss occurred only in the perirenal fat. Measurements of perfusion loss were only made in renal parenchyma because the registration was performed on the corresponding kidneys only. Perirenal adipose tissue was not registered and likely moves during the procedure due to changes in bowel position, therefore reliable measurements could not be made for adipose response to cryoablation.

Table 3: Mean Volume of Iceball and Perfusion Loss Regions Inside and Outside of Kidney

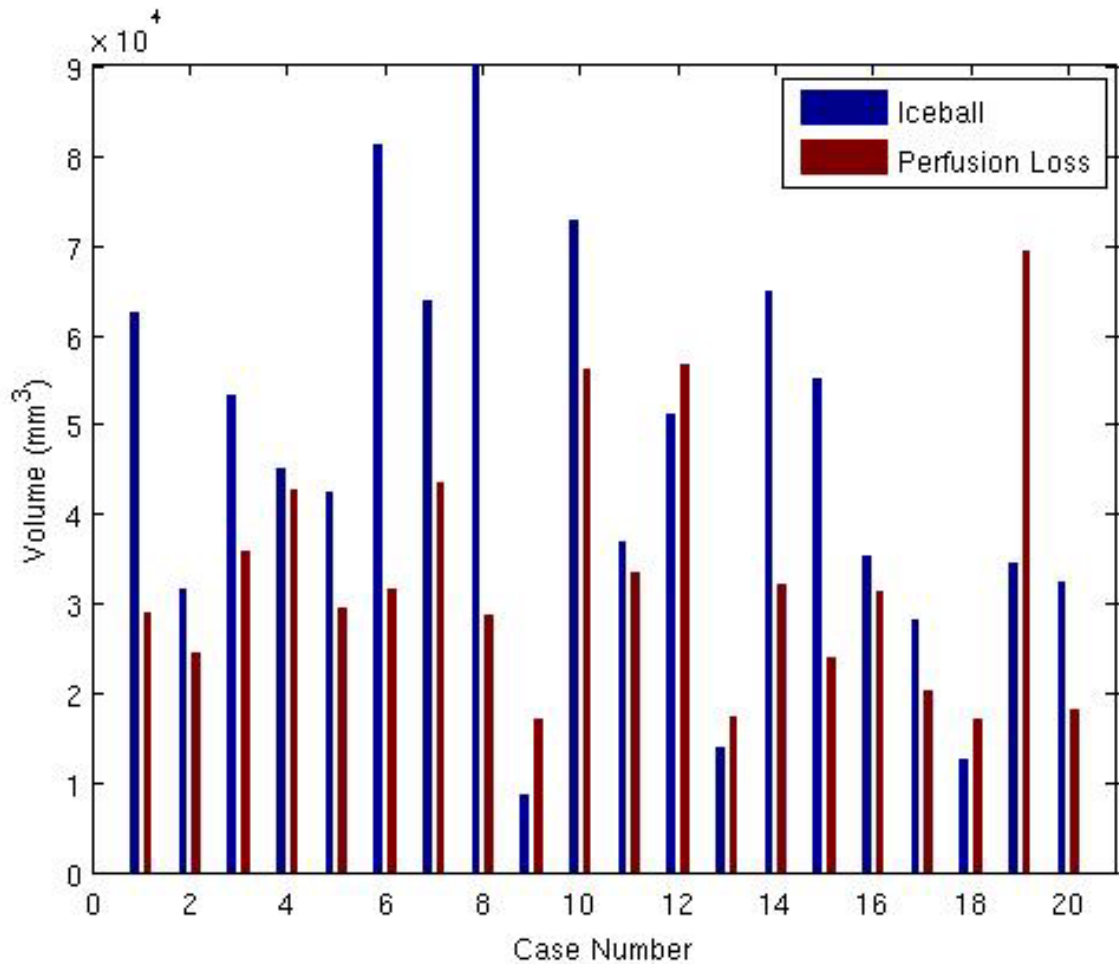| Region	Mean Diameter (mm)	Mean Volume (mm^3)
Tumor Volume	21.1 (10.4-40.4)	$4.93 \times 10^3 \pm 2.61 \times 10^3$
Perfusion Loss Total	39.8	$33.1 \times 10^3 \pm 14.4 \times 10^3$
Iceball Total	44.4	$46.0 \times 10^3 \pm 22.5 \times 10^3$

Figure 22: Observations of volumes of iceball and associated perfusion loss in all affected tissues for 20 cases

Perfusion loss around and within the iceball was measured at 1mm increments, starting at 5mm outside the iceball and ending at the center of the iceball. The perfusion loss fraction was calculated as the number of true pixels from the perfusion loss map at a distance as compared to the number of true pixels from the iceball map at that distance, illustrated in Figure 18. The perfusion loss fraction and positions around and within the iceball were modeled using MATLAB's glmfit with the logit link function.

To assess the goodness of fit of the logit model, the Pearson residuals from the model were tested to fit a normal distribution using the one-sample Kolmogorov-Smirnov test

[30]. For testing the Pearson residuals, the Kolmogorov-Smirnov test is described by the following:

H_0: the Pearson residuals follow a normal distribution

H_1: the Pearson residuals do not follow a normal distribution

The guiding principle behind the Kolmogorov-Smirnov test is to assess normality of the data by measuring the difference between the empirical cumulative distribution function and the known standard normal cumulative distribution function. This measurement is illustrated for data from this study in Figure 23. The logit function unique to these data is shown with the original perfusion loss fraction data in Figure 24.

Accuracy of Model

Manual registration of the patient data sets accounted for the rigid-affine transformations of rotation, scale, and translation differences. It was assumed that the kidney would not experience significant deformation during the procedure, so non-rigid deformable registration was not applied to these cases. Following vigilant manual registration, the final normal edge-to-edge distance was measured to determine the error in manual registration caused by organ deformation during the procedure or interpolation artifacts from volume resampling. The mean normal edge-to-edge distance between procedural steps across all 20 patient cases was 1.41±1.71mm. The standard error for the logit parameters from the iterative fitting was found to be ±0.0048 and ±0.0027 for α and β, respectively. The error in the logit parameters lead to uncertainty of ±0.02 mm in determining the LD_{95} distance. Therefore, registration error dominates as the source of uncertainty in the perfusion loss model.
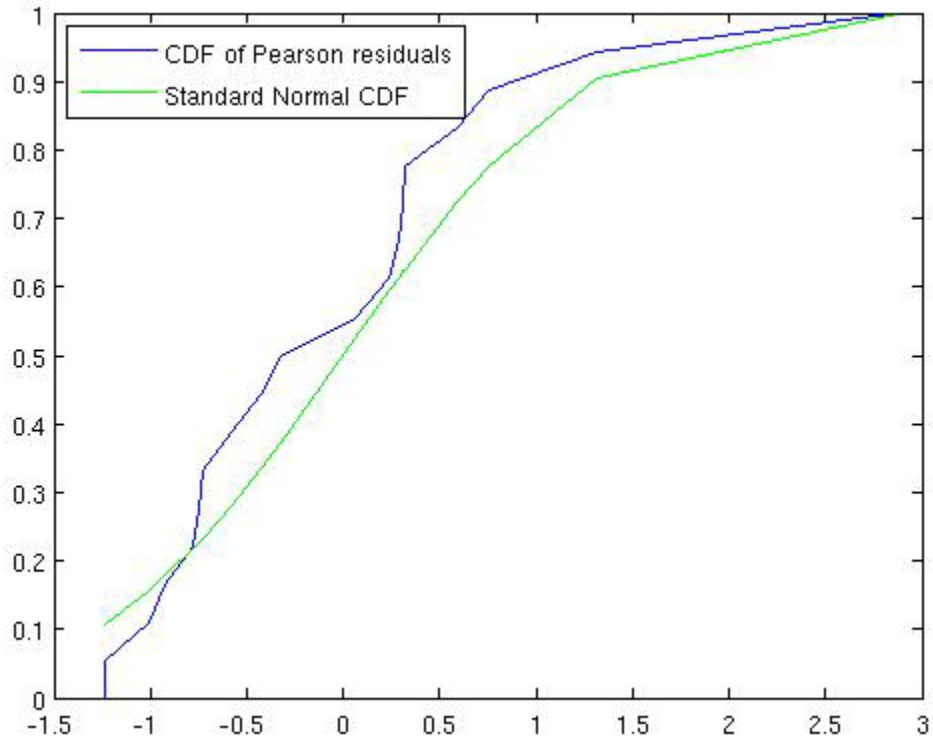
The empirical cumulative distribution function of the Pearson residuals agrees closely enough with the standard normal CDF that the null hypothesis could not be rejected, indicating that this model fits the data sufficiently well. The Kolmogorov-Smirnov test justified using the logit model to quantify perfusion loss likelihood within the iceball edges.

$$Prob(cell = non - perfused|distance\ in\ iceball = d) = \frac{e^{-0.4557+0.7942d}}{1 - e^{(-0.4557+0.792d)}}$$
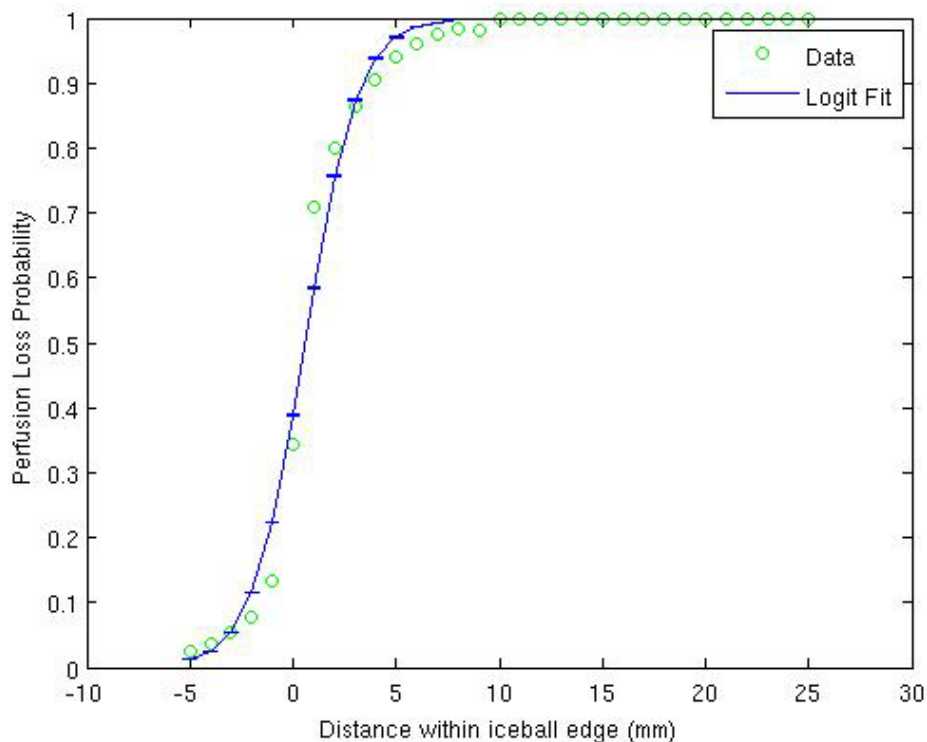
Figure 24: Model of Perfusion Loss within Iceball with Error Bars, 95% likelihood of perfusion loss occurs at 4.28mm within the iceball edge

Table 4: Results of logit fitting to perfusion loss fraction in iceball data

Logit Parameters	Logit Fit Results
α	-0.4557
β	0.7942
LD_{50} margin in iceball	0.57 mm
LD_{95} margin in iceball	4.28 mm

From the quantitative model, it was determined that a distance of 4.28±0.02 mm within the iceball edge, perfusion loss is 95% likely. Current clinical guidelines recommend that the iceball extend beyond the tumor margin by 3-5mm to effectively ablate the target tumor. This 3-5mm treatment margin is typically visually estimated by the radiologist during the procedure. Rather than relying on visual estimation, the logit model created here can be used to deliver a quantitative treatment margin that can be displayed as a contour on the planning image.

Measurement and final visualization of damage likelihood is heavily dependent on visualization of the iceball. In this study, the iceball was imaged using either a T2-weighted or T1/T2 ratio-weighted image. There were no iceball monitoring T1-weighted sequences available in the database. Therefore, the logit model and associated damage contours are only appropriate for use with T2-weighted images of the iceball. The damage likelihood estimation is based on distance within the iceball and does not account for tissue perfusion rates prior to the procedure.

This study was restricted to renal tissue that did not include collecting ducts; however surrounding peritoneal adipose tissue is also of interest to the radiologist. The contour display of damage is therefore only accurate within kidney tissue. Damage contours which extend beyond the kidney edge are erroneous and likely indicate poor registration between the monitoring and planning images. Characterization of response of the collecting ducts was not performed due to lack of data. Typically, cryoablation is prescribed for tumors at the poles of the kidney, distal to the collecting ducts. Therefore, the collecting ducts were infrequently treated by the iceball.

5.2 Specific Aim 2: Semi-Automated Perioperative Visualization of Target Coverage

The phase correlation registration was applied to artificial test objects as well as in-vivo data to test its accuracy under different circumstances (such as missing information) and to determine the execution time.

Test Images

Artificial binary test images were used for initial assessment of the automated phase correlation with Center of Mass subpixel registration. To determine the impact of pre-processing on registration accuracy, full images and edge-filtered images were tested. To

determine the impact of missing information, the moving image was incrementally deleted and registration accuracy was tested. In all cases, the moving test image was created by applying a random transformation to a copy of the reference image prior to applying registration. For these test objects, all were registered with final Hausdorff distance < 1 pixel.

The registration test using the complete binary test image is shown in Figure 27, where the left image shows the reference image (red) with the artificially shifted moving image (blue) and the right image shows the agreement between the reference and transformed objects (purple). The phase correlation with Center of Mass subpixel algorithm was tested for 50 random transformations. The mean Hausdorff distance before registration was 3.56±0.87mm with DSC 32.3% and the mean Hausdorff distance after registration was 0.67±0.31mm with 98.3% for the test object. The registration solver is sensitive to large misalignments and will not reliably recover translations greater than 16mm in any direction nor can it reliably correct for rotations greater than 15 degrees.

To determine the phase correlation method's robustness in the presence of missing information, the moving object was incrementally deleted. The missing information limit test using the partially deleted binary test image is shown in Figure 26, where the left image shows the reference image (red) with the partially-deleted moving image (green) and the right image shows the agreement between the reference and registered moving objects (yellow). The average Hausdorff distance before registration was 15.8±1.98mm with DSC 4.02±3.71% and average Hausdorff distance after registration was 1.98±0.17mm with DSC of 87.6±1.02% for object visibility ranging from 74.7% to 25.3%. Registration did not reliably recover transformations with less that 25% of the object visible, as demonstrated in Figure 25. This test with missing information established a lower limit of accuracy for registrations between images with missing information;

therefore, a registered Hausdorff distance of 1.98mm and DSC 87.6% is likely to be the

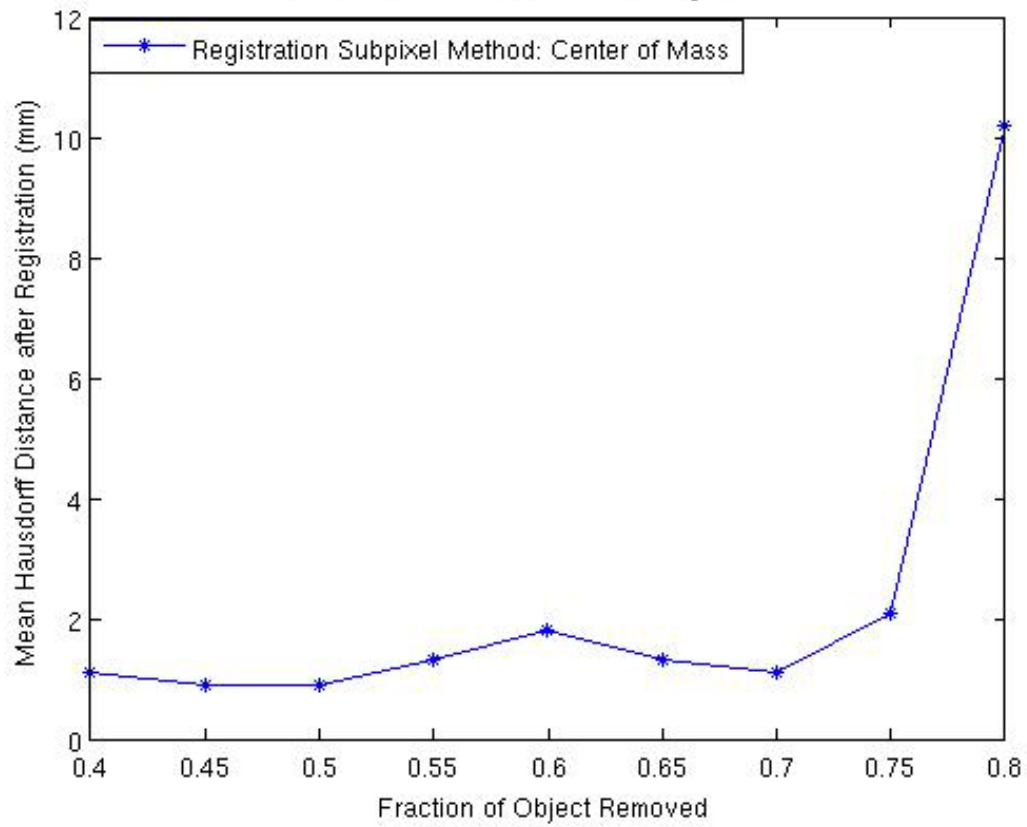most accurate registration that we can expect for in-vivo data.

Figure 25: Mean Hausdorff Distance after Registration versus Fraction of Object Deleted, registration of elliptical test objects remained successful until 75% of the moving object had been deleted. Based on this result, at 25% of the kidney needs to be visible on in-vivo images for successful registration

Figure 27: Test Objects Demonstrating successful registration; (left) Before (HD mean: 3.99mm) and (right) After Registration (HD mean: 0.67mm)


Figure 26: Missing Information test: Successful Registration with only 25.3% of the object visible (left) before registration with HD mean: 9.12 mm and (right) after registration (HD mean: 1.92mm after registration)

In-Vivo Data

Previously acquired in-vivo data were used for the final assessment of the automated registration. The phase-correlation registration solver was applied to the segmentation masks shown in Figure 30. Figure 32 compares the location of the unregistered and registered iceball with corresponding damage margins. In Figure 32(a), the planning and monitoring images are misaligned in the x and y directions as well as in the slice direction. In Figure 32(b), the registered iceball contour clearly indicates that the tumor is completely contained within the frozen region. Figure 33 shows several other visualizations of cases after successful registration. Figure 33 (a), (b), and (c) demonstrate cases with successful registration and good iceball segmentation, while (d) illustrates successful registration but poor iceball segmentation.

To test semi-automated segmentation and phase-correlation registration on in-vivo data, only 16 patients were used from the database. Out of the original 20, two cases were excluded due to a major error during the semi-automated segmentation step, one case was excluded due to large deformations present, and one case was excluded with <25% visible kidney during monitoring. An example of segmentation error due to low contrast boundaries at the kidney is shown in Figure 28 .
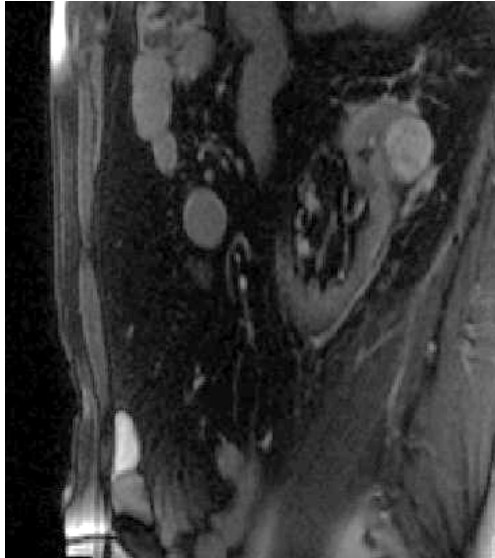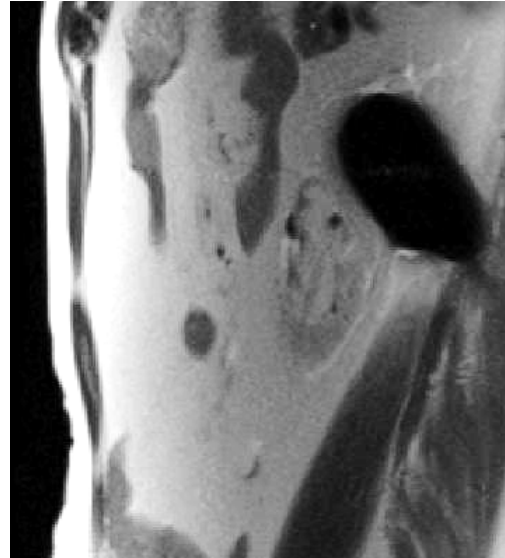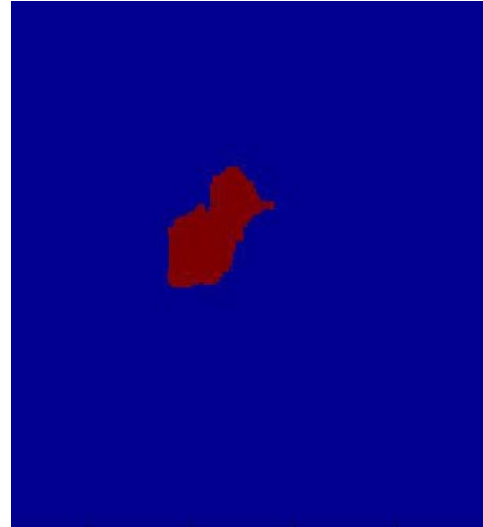
(a.i) Planning Image   (b.i) Monitoring Image
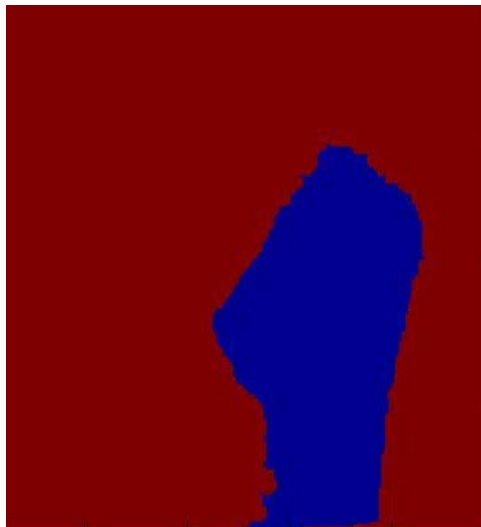
(a.ii) Segmentation Mask: Planning Image   (b.ii) Segmentation Mask: Monitoring Image

Figure 28: Example of segmentation failure due to low contrast boundaries in the kidney (a.i) original sagittal bssFP planning image showing kidney and target tumor; (a.ii) erroneous segmentation mask resulting from low contrast and non-uniformity in the kidney visualized on the planning image; (b.i) original sagittal ssFSE monitoring image showing kidney and iceball at final freeze point; (b.ii) erroneous segmentation mask due to very low contrast between kidney and surrounding peritoneal tissue.

The computation time for each component of the visualization tool is described below in

Table 5. In total, all MATLAB functions complete within 2 minutes for planning and

monitoring images with dimensions 256x256x50 (typical dimensions for this database).

Component	Image Size	Execution Time
Random Walker Segmentation	256x256x50 147 seed points	11.4 s
Phase Correlation Zero Padded Method	*256x256x50*	*11.3 s*
Phase Correlation Center of Mass Method	256x256x50	0.42 s
Registration Module Center of Mass Only	256x256x50 2 image stacks	14.4 s
Segmentation Module	256x256x50 2 image stacks 375 seed points	76.7 s

Appropriateness of Rigid Registration

Rigid registration accounts for misalignments due to translation, rotation, and scaling, but does not consider any fluid transformations or deformations. Therefore, the major assumption made is that the kidney does not experience significant deformations between the planning and monitoring steps of cryoablation. To validate this assumption, deformations were measured between kidney edges in the planning and monitoring steps of the procedure. Deformations were not measured on evaluation images because the evaluation images are not used in perioperative visualization. The average observed deformation in each case is shown in Figure 29. Deformation measurements were made from the manually registered segmentation maps created for SA1 between in-tact kidney edges (iceball obscured edges in monitoring images were not included). A normal vector was defined for each edge point on the planning segmentation mask by searching for the nearest point in either direction (inside or outside the kidney edge) on the monitoring mask along the normal. Deformations were defined as any non-zero distance between corresponding points along the normal search vector.
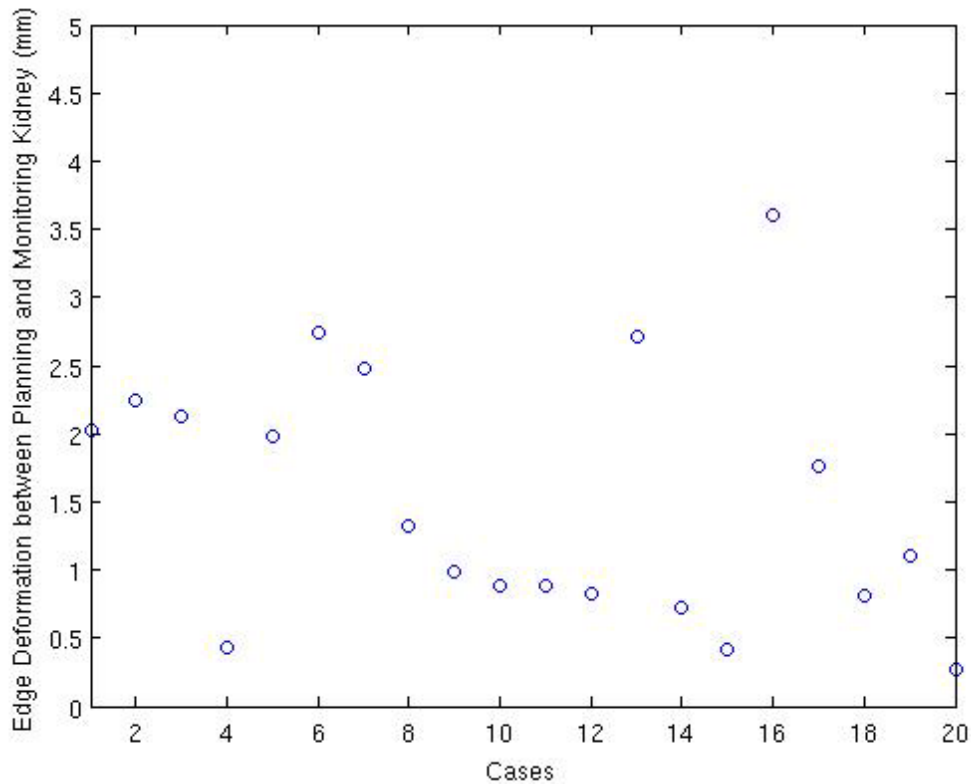
Figure 29: Average deformation observed between kidney on planning images and kidney on monitoring images across 20 patient cases. Iceball-obscured kidney edges in monitoring images were not considered in the deformation measurement.

The mean deformation across all 20 patient cases was 1.41±1.71mm. The proposed registration technique did not correct for the deformations. Therefore the accuracy of the rigid registration was limited by the presence of the observed deformations. Considering the average misalignment after registration observed in the test objects with missing information (1.9mm) and the presence of deformations (1.4mm), successful registration was defined as a mean Hausdorff distance of 3.3mm across the 16 in-vivo cases. Registration results and prior deformations are shown in Figure 30 for all cases, including the four that were excluded. Note that case 15 had too much kidney missing and could not be registered; case 16 had large deformations, which prevented successful registration, and cases 9 and 11 failed due to segmentation errors at low-contrast boundaries.

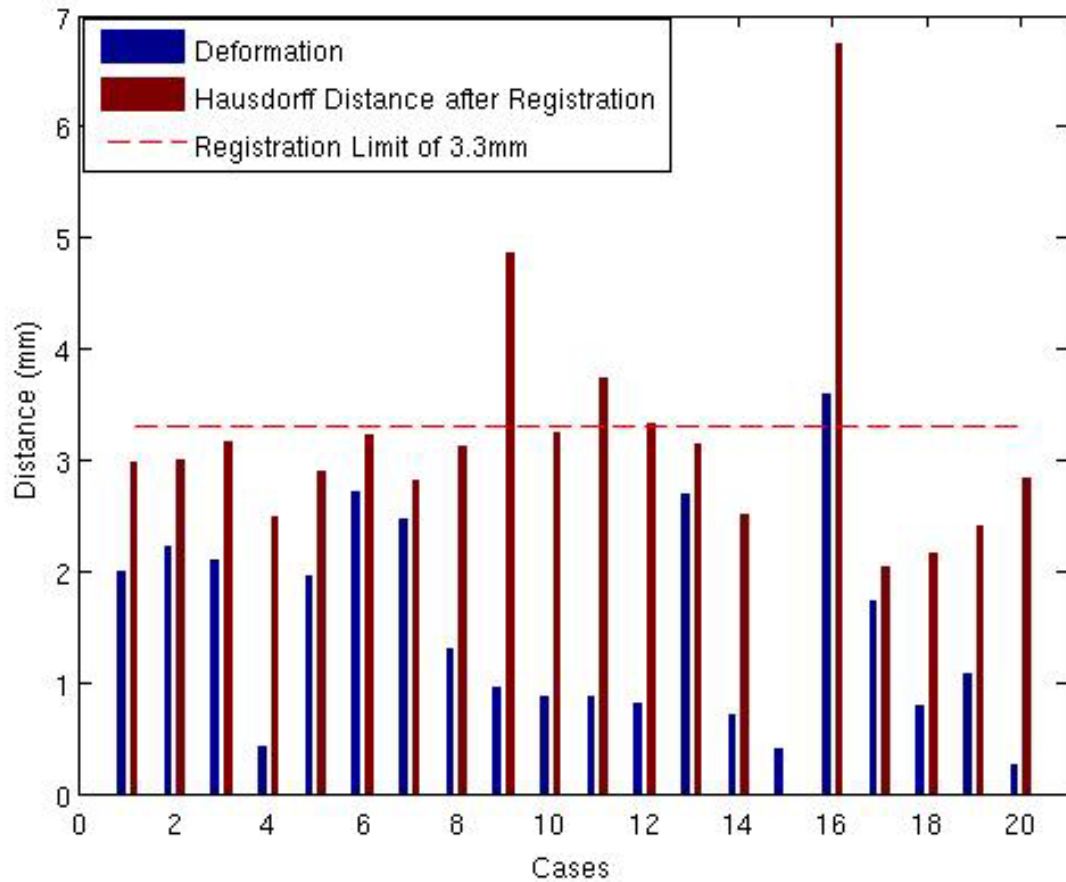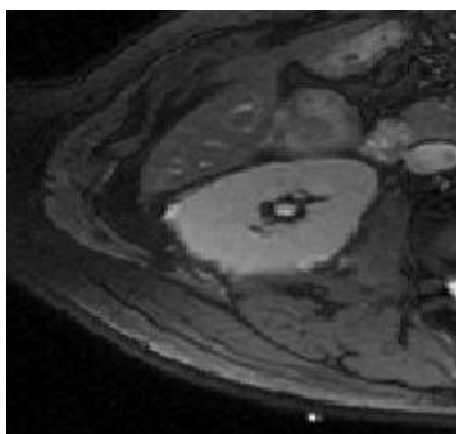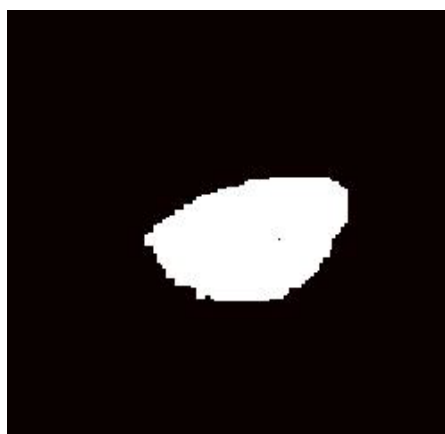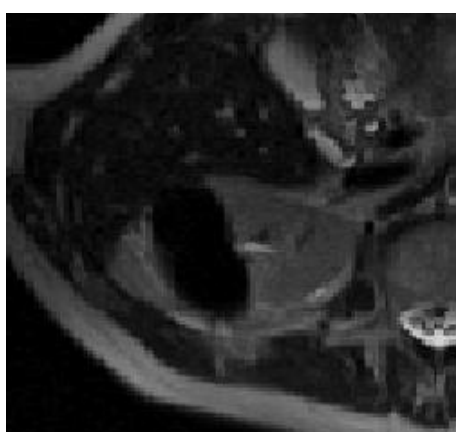| Segmentation Masks: Planning vs. Monitoring	Mean Hausdorff Distance	Dice Similarity Coefficient
Before Registration	7.4 – 15.8 mm	46.6±23.2%
After Registration	2.05 – 3.31 mm	82.6±.5%

Figure 30: Comparison of Deformation and Registration Results for 20 In-vivo Cases, note that case 15 had too much kidney missing and could not be registered, case 16 had large deformations which prevented successful registration, cases 9 and 11 failed due to segmentation errors at low-contrast boundaries.
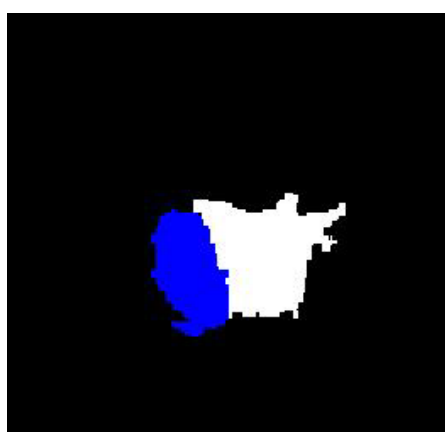
(a.i)

(a.ii)

(b.i)

(b.ii)

Figure 31: Comparison of in-vivo images and associated segmentation masks used in the registration solver; (a.i) original planning image, slice 15, where planning and monitoring series were initially aligned prior to registration. (a.ii) Planning segmentation mask, kidney (white), following random walker segmentation; (b.i) Monitoring Image, slice 15, showing iceball and misaligned anatomy compared to planning slice 15; (b.ii) Monitoring segmentation mask, kidney (white) used for registration solver and iceball (blue), following random walker segmentation.
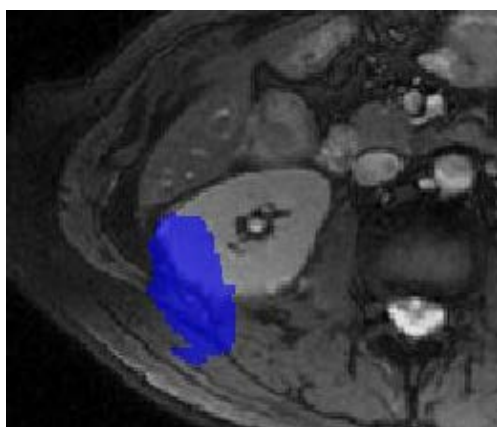

(a)
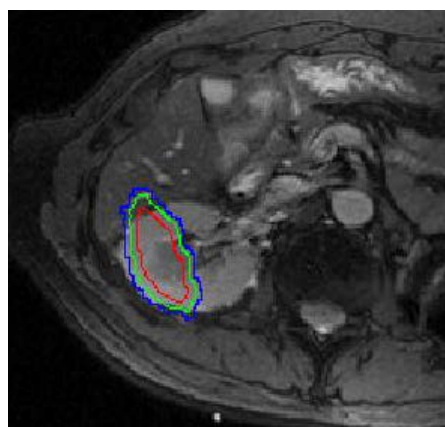
(b)

Figure 32: Comparison of apparent iceball location with respect to the planning image before and after registration; (a) unregistered iceball location with respect to planning image. Iceball is displaced in all 3 dimensions, especially the slice direction. (b) Registered iceball contour (blue) and modeled damage probabilities (green = 50%, red = 95%) projected on planning image

5.2.1 Limitations

From these studies, it was determined that the registration fails when less than 25% of the object-to-be-registered is visible. Therefore, this registration approach will not be appropriate in cases where more than 80% of the kidney is obscured by the iceball at maximum freeze time. Judging from the in-vivo data that were analyzed for this study, only 1 out of 16 cases fell into the category of more than 75% kidney obscured during freeze.

Another limitation of the phase correlation technique is that the objects to be registered must be very close to identical to achieve the most accurate registration. For the clinical application, the organ of interest must remain as constant as possible during the procedure, which may require breath-holding and sedation. This registration approach is not appropriate for organs that suffer significant deformations during a procedure and should only be applied in cases where the amount of organ deformation can be minimized.
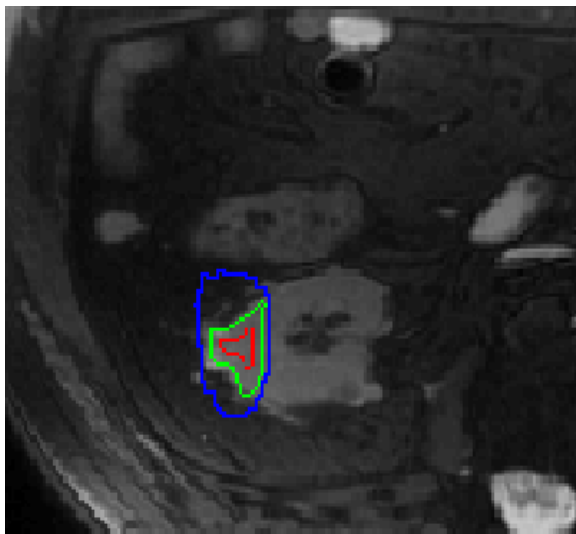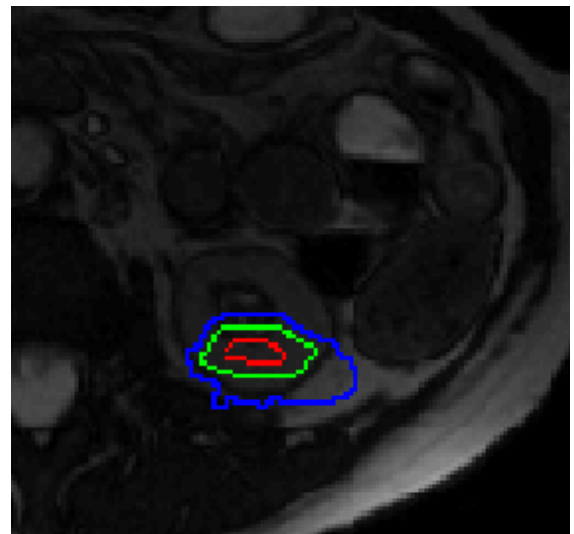
(a)   (b)
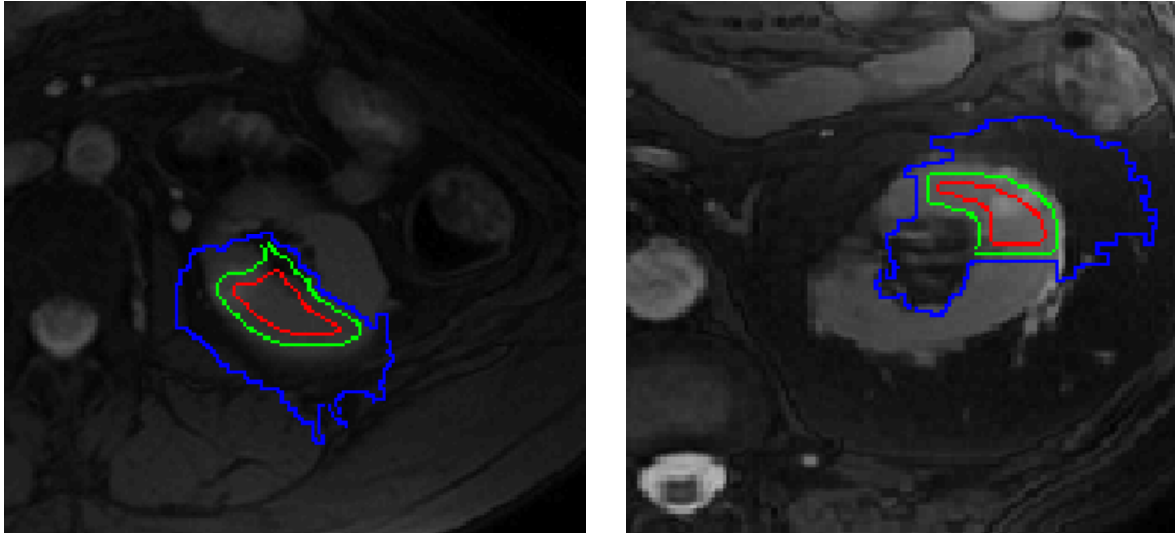
(c)   (d)

Figure 33: Visualization of Iceball and Damage Contours (green = 50%, red = 95%) after successful registration; (a), (b), and (c) illustrate good registration and good segmentation; note that (d) has some segmentation error present that causes the iceball contour to appear to spread into the center of the kidney

6   Conclusions and Future Directions

6.1 Summary of Work

Through a retrospective study of 20 patient cases, the relationship between the likelihood of perfusion loss in renal parenchyma and distance within iceball used for cryoablation treatment was quantified and iteratively fit to a logit curve. Using the parameters from the logit fit, the margin for 95% perfusion loss likelihood was found to be 4.28 mm within the iceball. The observed margin corresponds well with the clinically accepted margin of 3-5mm within the iceball.

In order to display the iceball position and perfusion loss likelihood to the radiologist, algorithms were implemented to create a fast segmentation and registration module which executed in under 2 minutes, within the clinically-relevant 3 minute monitoring period. The registration solver is robust to missing information and is successful within the established bounds of registered Hausdorff distance < 3.3 mm and Dice Similarity Coefficient > 70%.

Using 16 patient cases, the average Hausdorff distance was reduced from 10.1mm to 2.94 mm with average DSC increased from 46.6% to 82.6% before and after registration.

Measurement and final visualization of damage likelihood is heavily dependent on visualization of the iceball. In this study, the iceball was imaged using either a T2-weighted or T1/T2 ratio-weighted image. There were no iceball monitoring T1-weighted sequences available in the database. Therefore, the logit model and associated damage contours are only appropriate for use with T2-weighted images of the iceball. The damage likelihood estimation is based on distance within the iceball and does not account for tissue perfusion rates prior to the procedure.

Accurate display of the iceball and the damage contour is dependent on accurate registration. As mentioned previously, segmentation error is likely to cause failure of the registration solver. Segmentation error will attribute non-kidney regions to the final segmentation mask, resulting in erroneous shapes and boundaries. Failure of the registration then occurs because the visible kidney regions need to be as similar as possible in order to accurately compare the spatial shift between the two images. By the same principle, the presence of large deformations in the kidney during the procedure or very little kidney visible around the iceball will also lead to registration failure. In the case of obscured kidney, the image stack should be acquired in another orientation to elucidate more of the organ.

Finally, this periprocedural visualization tool is not a replacement for the supervision and assessments of the attending radiologist. The visualization tool is intended to provide meaningful information regarding iceball position in relation to target lesion position along with a likelihood of damage caused by the iceball. Such visualization and information is likely to streamline the radiologist's decision and the overall cryoablation procedure.

6.2 Future Directions

6.2.1 Streamlining the Tool for Clinical Use

The following changes should be implemented before this tool can be wholly appropriate

for periprocedural use in renal cryoablation.

Implement a fully automated pre-processing or segmentation that is more robust and

more efficient to replace the semi-automated Random Walker segmentation technique. In

this study, this approach was found to perform poorly in the presence of low contrast

boundaries. Furthermore, this segmentation approach, as it is currently available, is only

appropriate for 2D segmentation. Ideally, the visualization tool would incorporate a

multislice or 3D technique for robust segmentation.

If possible, the imaging protocol for cryoablation would be standardized, including a 3D

gradient-recalled echo sequences in order to improve the rotational registration.

Incorporating 3D acquisitions into the visualization tool would eliminate the need to

resample the acquired data into separate volumes to simulate different orientations,

thereby increasing efficiency and decreasing uncertainties due to interpolation artifacts.

For full periprocedural functionality, scanner compatibility with MATLAB must be

considered. Not all (if any) interventional MRI scanners currently support interfacing with

MATLAB. If necessary, the approaches used by the visualization tool would be translated

to a compatible language such as C++ before beginning clinical implementation.

6.2.2 Extending the Tool to More Targets

Ideally, this tool could be used during any cryoablation procedure to aid in adaptive

planning. In order to generalize this tool, future work needs to be done to achieve the

following aims.

Cryoablation is performed in several in other tissues such as liver, prostate, and bone.

Damage models for each tissue type would be created via retrospective studies. Prior

tissue perfusion rates should also be considered to develop more accurate treatment response models.

This study quantified perfusion loss likelihood within the iceball. To give relevant feedback during the procedure, the predictive capability of the damage model should be assessed using a separate data pool.

7 References

[1]   Autorino R, Kaouk JH. Cryoablation for small renal tumors: Current status and future perspectives. Urologic Oncology 2012;30:S20–7.

[2]   Hines-Peralta A, Goldberg SN. Radiofrequency Ablation and Cryoablation for Renal Cell Carcinoma. In: Atkins M, Dizon D, editors. UpToDate, Waltham, MA: Wolters Kluwer Health; 2011.

[3]   Gill IS, Remer EM, Hasan W a, Strzempkowski B, Spaliviero M, Steinberg AP, et al. Renal cryoablation: outcome at 3 years. Urology 2005;173:1903–7.

[4]   Ahrar K, Ahrar J, Javadi S, Pan L. Real-Time Magnetic Resonance Imaging-Guided Cryoablation of Small Renal Tumors at 1.5 T. Investigative Radiology 2013;48:437–44.

[5]   Aetna Incorporated. Clinical Policy Bulletin No. 0100: Cryoablation. 2013.

[6]   Uchida M, Imaide Y, Sugimoto K, Uehara H, Watanabe H. Percutaneous cryosurgery for renal tumours. British Journal of Urology 1995;75:132–6.

[7]   Rosenberg MD, Kim CY, Tsivian M, Suberlak MN, Sopko DR, Polascik TJ, et al. Percutaneous cryoablation of renal lesions with radiographic ice ball involvement of the renal sinus: analysis of hemorrhagic and collecting system complications. American Journal of Roentgenology 2011;196:935–9.

[8]   Bang HJ, Littrup PJ, Goodrich DJ, Currier BP, Aoun HD, Heilbrun LK, et al. Percutaneous cryoablation of metastatic renal cell carcinoma for local tumor control: feasibility, outcomes, and estimated cost-effectiveness for palliation. Journal of Vascular and Interventional Radiology 2012;23:770–7.

[9]   Van den Bosch M a a J, Josan S, Bouley DM, Chen J, Gill H, Rieke V, et al. MR imaging-guided percutaneous cryoablation of the prostate in an animal model: in vivo imaging of cryoablation-induced tissue necrosis with immediate histopathologic correlation. Journal of Vascular and Interventional Radiology 2009;20:252–8.

[10]   Li X, Nail SL. Nuclear Magnetic Resonance Imaging of Freeze-Drying. Journal of Pharmaceutical Sciences 2006;95:2516–25.

[11]   Huttenlocher D. Comparing images using the Hausdorff distance. Pattern Analysis and Machine Intelligence 1993;15.

[12]   Zou KH, Warfield SK, Bharatha A, Tempany CMC, Kaus MR, Haker SJ, et al. Statistical validation of image segmentation quality based on a spatial overlap index. Academic Radiology 2004;11:178–89.

[13]   Zitová B, Flusser J. Image registration methods: a survey. Image and Vision Computing 2003;21:977–1000.

[14]   Stalling D, Westerhoff M, Hege H. Amira - a Highly Interactive System for Visual Data Analysis 2005;1:1–18.

[15]   Chen Q, Defrise M, Deconinck F. Symmetric Phase-Only Matched Filtering Image Registration and Recognition. IEEE Transactions on Pattern Analysis and Machine Intelligence 1994;16.

[16]   Pfluger T, Vollmar C, Wismüller A, Dresel S, Berger F, Suntheim P, et al. Quantitative comparison of automatic and interactive methods for MRI-SPECT image registration of the brain based on 3-dimensional calculation of error. Journal of Nuclear Medicine 2000;41:1823–9.

[17]   Woods RP, Grafton ST, Watson JD, Sicotte NL, Mazziotta JC. Automated image registration: II. Intersubject validation of linear and nonlinear models. Journal of Computer Assisted Tomography 1998;22:153–65.

[18]   Wyngaerd J Vanden, Gool L Van, Koch R, Proesmans M, Leuven B-, Zentrum ETH, et al. Invariant-based registration of surface patches. The Proceeding of the 7th IEEE International Conference on Computer Vision 1999:1–6.

[19]   Sharp G, Lee S, Wehe D. ICP registration using invariant features. Pattern Analysis and Machine Intelligence 2002;24:90–102.

[20]   Studholme C, Hill DLG, Hawkes DJ. An overlap invariant entropy measure of 3D medical image alignment. Pattern Recognition 1999;32:71–86.

[21]   Veugen L, Meier D. Image Registration: Techniques, Benchmarking, Strategy. Boston, USA: 2010.

[22]   Van den Dool R. Image Processing Tools: Fourier-Mellin Transform. 2013.

[23]   Liu X, Tuncali K. Fully automatic 3D segmentation of iceball for image-guided cryoablation. 34th Annual Internation Conference of the IEEE EMBS, San Diego: 2012, p. 2327–30.

[24]   Warfield S, Zou K, Wells W. Simultaneous truth and performance level estimation (STAPLE): an algorithm for the validation of image segmentation. IEEE Transactions on Medical Imaging 2004;23:903–21.

[25]   Grady L. Random walks for image segmentation. IEEE Transactions on Pattern Analysis and Machine Intelligence 2006;28:1768–83.

[26]   Pichon E, Tannenbaum A, Kikinis R. A statistically based flow for image segmentation. Medical Image Analysis 2004;8:267–74.

[27]   Cardoso MJ, Melbourne A, Kendall GS, Modat M, Robertson NJ, Marlow N, et al. AdaPT: An adaptive preterm segmentation algorithm for neonatal brain MRI. NeuroImage 2013;65:97–108.

[28]   Warfield SK, Zou KH, Wells WM. Simultaneous truth and performance level estimation (STAPLE): an algorithm for the validation of image segmentation. IEEE Transactions on Medical Imaging 2004;23:903–21.

[29]   Foroosh H, Zerubia JB, Berthod M. Extension of phase correlation to subpixel registration. IEEE Transactions on Image Processing 2002;11:188–200.

[30]   Trinity. Introduction to Generalized Linear Models. Introduction to Statistical Modeling, Oxford: University of Oxford; 2002, p. 1–10.

Vita

Katherine Dextraze is a Medical Physics Specialized Master's student in the Graduate School of Biomedical Sciences at University of Texas Health Science at Houston. She will continue her educational journey as a Ph.D. student starting in August 2013.

Katherine began her research career while attending high school at the South Carolina Governor's School for Science and Mathematics. After her junior year, she worked as a summer intern at Clemson University in the department of Chemical Engineering. She received her Bachelor of Science in Nuclear and Radiological Engineering from Georgia Institute of Technology. At Georgia Tech, Katherine was involved as an undergraduate teaching assistant for Physics I and II, financial committee chair for the 2011 American Nuclear Society Student Conference, and an undergraduate researcher in medical physics. Before enrolling in graduate school in August 2011, Katherine spent the summer working as a Halle Fellow in the Comprehensive Pneumology Center at the Helmholz-Zentrum in Munich, Germany.

Katherine's interest in student leadership has continued at UT Health Science Center at Houston. She has served on the Medical Physics Student Council and taken part in orientation and recruitment for interviewing students. Recently, she has been elected to the Student Inter-Council for the UT Health Science Center at Houston, to the Graduate Student Association as its President, and serves as the IT/Communication Co-Chair for the Student and Trainee Working Group within the American Association of Physicists in Medicine.

Permanent Address:

1915 Calumet Street

 Houston, TX 77004